OPTICAL LIMITING AND FIELD EMISSION STUDIES OF CARBON NANOTUBES

GOHEL AMARSINH

NATIONAL UNIVERSITY OF SINGAPORE

2004

OPTICAL LIMITING AND FIELD EMISSION STUDIES OF CARBON NANOTUBES

GOHEL AMARSINH

B.Sc. (Hons.)

SUPERVISOR

A/PROF ANDREW WEE

THESIS SUBMITTED

FOR THE DEGREE OF MASTER OF SCIENCE

DEPARTMENT OF PHYSICS

NATIONAL UNIVERSITY OF SINGAPORE

2004

Table of Contents

Abstract

In this research, we investigate two of carbon nanotubes' most well known properties: optical limiting and field emission. Our aim is to modify the carbon nanotubes using physical and chemical means to modify their optical limiting and field emission characteristics.

In the first part of this thesis, we coat randomly aligned multi-walled carbon nanotubes (MWNTs) with a-Au and a-Ag nanoparticles. The optical limiting characteristics of as-grown MWNTs and the coated MWNTs are then measured and compared at 532nm and 1064nm using a nanosecond laser. It is observed that, at 532nm, the coated MWNTs show better optical limiting characteristics compared with the original MWNTs while there is no observable enhancement at 1064nm. We propose surface plasmon absorption of the a-Au and a-Ag nanoparticles on the coated MWNTs to be the mechanism responsible for the improvement in optical limiting. UV spectrum of the samples and non-linear scattering measurements further confirmed the validity of this mechanism.

In the second part of the thesis, we modify the MWNTs by plasma etching with N_2 and Ar for 10min and 20min each. The field emission characteristics of the etched samples are then measured using a custom-made chamber and compared to that of MWNTs. The N_2 etched MWNTs showed great improvement in field emission properties, while the Ar etched MWNTs displayed poorer field emission characteristics compared to the parent MWNTs. Various methods of characterization, such as XPS, PES, SEM and Raman spectroscopy are used to investigate these observations and an explanation to our results is proposed.

Chapter 1: Introduction

In this chapter, an introduction to carbon nanotubes is provided. Although their properties and synthesis methods are widely studied and well known, carbon nanotubes are central to this project, thus an extensive treatment is provided.

1.1 Carbon

Carbon is the sixth element in the periodic table and the lightest of the Group IV elements. Owing to carbon's unique electronic configuration: ($1s^2$, $2s^2$, $2p^2$), it has many distinct properties that set it apart from other Group IV elements such as silicon and germanium. This is mainly due to the fact that carbon is able to undergo sp^1, sp^2 and sp^3 hybridisation (other Group IV elements only form sp^3 bonding). This allows carbon to readily bond with many other elements to form a variety of compounds, and also allows carbon to exist in many different forms of allotropes, such as graphite and diamond.

Carbon has interested researchers since the 19^{th} century when Thomas A. Edison used a carbon fiber as the filament for the first electric bulb (1). Although the much more effective tungsten filament soon replaced the carbon fiber filament, development of the carbon fiber proceeded rapidly through the efforts of researchers round the world. A major stimulus for carbon research started in the 1950s when the space and airline industry brought about an increased demand for strong, stiff and lightweight fibers (1). This served as a catalyst for developments in carbon fiber preparation techniques based on polymer precursors. The carbon whisker was also synthesized during this period, which became the benchmark for carbon fiber properties. Through continual efforts by researchers and improvements in technologies, synthesis methods were being perfected

as defects of synthesized fibers were reduced and properties enhanced. With the invention of the catalytic vapour deposition process, researchers now had greater control of the fabrication process.

As the dimensions of the carbon fibers continue to decrease, questions are being asked as to if there exists a lower limit. Then came the discovery of fullerenes by Kroto and Smalley, which paved the way for nanoscale carbon fibers (2). As fullerene synthesis techniques were being improved upon, there was much speculation of the existence of carbon fibers with the dimensions comparable to that of fullerenes. The breakthrough came with S. Ijima's discovery in 1991, when he observed the first nanoscale carbon nanotube using transmission electron microscopy (3).

1.2 Properties of Carbon

The uniqueness of carbon stems from the fact that it is able to undergo various forms of hybridisation that allows it to form various allotropes. In ambient conditions, the stable graphite phase is formed, with carbon atoms in a planar sp^2 bonding arrangement. Under high pressure and temperature, carbon switches to tetrahedral sp^3 bonding forming diamond, which continues to remain largely stable after the release of pressure.

Properties of carbon vary differently when in the graphite state and in the diamond state. Graphite exhibits metallic behaviour in the intra-plane direction but poor electrical conductivity in the inter-plane axis (4). Graphite is also the stiffest material known, having the highest in-plane elastic modulus. On the other hand, diamond shows wide-gap semiconductor behaviour, and is the hardest known material (5). Diamond also has the highest atomic density of any known solid.

Of all the fullerenes, icosahedral C_{60} is the most stable and common (6). Within the shell, the carbon atoms mostly form sp^2 bonding, although some sp^3 bonding is present as well to accommodate the curvature of the shells. The second most common fullerene is C_{70}, which is formed from C_{60} by adding five hexagons around the equator of the C_{60} shell, and rotating the two halves of the C_{60} shell by 36^0 with respect to each other to form the rugby-shaped fullerene. It is interesting to note that the average carbon-carbon bond distance is approximately 1% larger than that of graphite; hence one would expect the properties of fullerenes to mirror closely with graphite.

1.3 Carbon Nanotubes

Carbon nanotubes are essentially one-dimensional tubular fullerenes, with nanometer diameters and properties similar to that of graphite fibers. They can be visualized to be formed by rolling up a graphene sheet into a cylinder. Carbon nanotubes have shown remarkable properties that made it one of the most exciting materials in the past decade (3). They have a high aspect ratio, incredible mechanical strength and excellent electrical properties, giving them the possibility of being employed in various diverse applications such as hydrogen storage, scanning tunnelling microscopy tips and field emission displays.

The uniqueness of the carbon nanotube structure is attributed to the helicity in the arrangement of carbon hexagons on the surface layer honeycomb lattice. The helicity, which is determined by symmetry and tube diameter, introduces modifications to the electronic density of states, hence giving the nanotubes a unique electronic character (3). Meanwhile, the topology of the carbon nanotubes has important effects on their physical

properties. In fact, there have been theoretical reports suggesting the existence of strong structure-property correlation, bringing new excitement to the study of this material (7).

1.4 Structure of Carbon Nanotubes

There are essentially two broad categories of carbon nanotubes: single-walled and multi-walled. Single-walled carbon nanotubes (SWNT) were first reported in 1993, and are essentially singular graphene cylindrical walls with diameters that range between 1~2nm (8). Multi-walled carbon nanotubes (MWNT), first observed by Ijima in 1991, consist of several nested cylinders that have an interlayer spacing of 0.34nm, much like the interlayer distance of bulk graphite. There is no three-dimensional ordering between the individual graphite layers, unlike that of graphite, suggesting that the interlayer structure is turbostratic. The outer wall diameters can be as large as 50nm while the inner hollow has a diameter of up to 8nm.

There are several ways in which a graphene sheet can be rolled up to a cylinder to form a single-walled nanotube (9). The boundary conditions around the cylinder are satisfied only when one of the Bravais lattice vectors in the plane of the graphene sheet maps to the complete circumference of the cylinder. The Bravais lattice vectors are formed by the linear combination of two primitive lattice vectors (Fig. 1.1) (10),

$$\boldsymbol{R} = m\boldsymbol{a_1} + n\boldsymbol{a_2} \quad (1)$$

Hence, the structure of a SWNT can be described by the integer pair (*m*, *n*).

Different SWNT structural configurations can be produced. A zig-zag tube, (*n*, *0*), or armchair tube, (*n*, *n*), is obtained when the sheet is rolled up along one of the symmetry axis (8). The graphene sheet can also be rolled up in a direction away from the symmetry

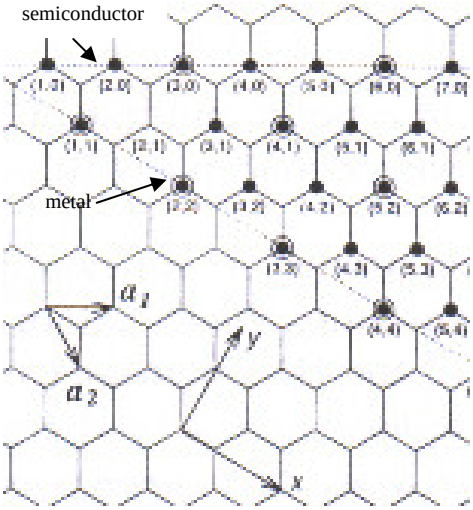

Fig 1.1: Possible vectors defined by the integer pair (m, n) for different classes of nanotubes (Adopted from (10)).

axis. This forms a chiral nanotube (*m*, *n*), in which the atoms in a unit cell are aligned in a spiral. Besides differing in terms of chiral angle, nanotubes also differ in diameter. Hence, a nanotube is commonly characterized by its diameter d and chiral angle θ, which are defined as follows:

$$d = \left(a\left(n^2 + m^2 + nm\right)^{1/2}\right)/\pi \qquad (2)$$

$$\theta = ar\cos\left[\sqrt{3}(n+m)/2\left(n^2 + m^2 + nm\right)^{1/2}\right] \qquad (3)$$

Such a diversity of structural configurations is commonly found in practice, and there is no particular preference as to which type of nanotube is formed (8). In most circumstances, the walls of MWNTs are chiral (3) and have different helicities (11). Both SWNTs and MWNTs have high aspect ratios, with ~µm lengths and diameter ranging from ~1nm for SWNTs to ~50nm for MWNTs.

If SWNTs were formed by rolling up a graphene sheet, then they would be open-ended. However, pristine SWNTs are mostly observed to be capped at both ends by fullerene half-spheres that contain both pentagons and hexagons (9). TEM images of a SWNT show a well-defined spherical tip while that of a MWNT show a more polyhedral cap. Sometimes, open-ended nanotubes can be observed. Such situations occur when the cap of the nanotube is removed and the ends of the graphene layers and internal cavity of the tube is exposed.

Defects can also be present in the hexagonal lattice body of the carbon nanotube in the form of pentagons and heptagons. Pentagon defects are mostly found at the cap and produce a positive curvature of the graphene layer. Negative curvatures of the tube walls are due to the presence of heptagonal defects (12). Sometimes, these defects can be formed by several pentagons or heptagons forming together, or even in combination. These defects alter the shape and dimensions of the nanotubes without causing any strain in the structure through lattice distortions. The end result is the alteration of helicity of the nanotubes by the insertion of junctions, which allow nanotubes of different electronic structure to be linked (13).

1.5 Electronic Structure of Carbon Nanotubes

Much has been studied about the electronic structure of SWNTs. Research has shown that the electronic properties vary in a predictable way from metallic to semiconducting with structural variations, which is due to the unique band structure of graphene (14). Graphene is a zero-gap semiconductor as the energy bands of its p-electrons cross the Fermi level at the Brillouin zone edges (8). Although it should behave

like a metal at room temperature, in reality it shows a semi-metallic behaviour because the electron density at the Fermi level is quite low (15). When the graphene sheet is rolled up to form a cylinder, periodic boundary conditions are imposed at the circumference, which limits the number of electron wave vectors perpendicular to the tube axis. When these wave vectors cross the edge of the Brillouin zone, the carbon nanotube is metallic in nature. All armchair tubes and one third of zig-zag and chiral tubes are metallic. For the rest of the nanotubes, they all show a gap in their band structure, thereby exhibiting semiconductor behaviour, with a band gap that scales inversely with the tube radius. For zig-zag and chiral metallic nanotubes, there is actually a small band gap due to hybridisation effects caused by tube curvature in very small tubes. This is not observed in armchair nanotubes as they are strongly metallic.

The experimental evidence for these theoretical predictions came only in 1998 with scanning tunnelling spectroscopy (16, 17). Conductivity measurements have shown that SWNTs act as coherent quantum wires where the conduction takes place via discrete electron states. Transport measurements show that the coherence lengths in SWNTs are extremely long (18). MWNTs also show similar effects although they have multiple shells and larger diameters.

1.6 Synthesis Methods of Carbon Nanotubes

1.6.1 Arc Discharge

The arc discharge was the first method used for the production of SWNTs and MWNTs (3). In fact, it was at the ends of graphite electrodes used in an electric arc discharge where Ijima first observed carbon nanotubes. Since this method has been used

for the synthesis of carbon fibers, it is possible that nanotubes were already observed before 1991 but were not identified (19). An arc is struck between two graphite electrodes in He gas atmosphere at typical conditions of 16V bias and currents of up to 80A at 400mbar pressure. MWNTs produced using this method are long, straight tubes that are closed at both ends. By using an arc discharge with a cathode containing Ni or Fe catalysts and graphite powder mixture, SWNTs can be synthesized. The yield of the SWNTs has been increased over the years by optimising the catalyst mixture and deposition conditions (20).

1.6.2 Laser Ablation

Laser ablation was first demonstrated to synthesize SWNTs in 1996 (21). The synthesis is carried out in a horizontal flow tube in the presence of an inert gas flow. The laser is used to vapourize the transition metal graphite composite electrode target at temperatures up to 1200^0C. Two laser pulses are used in the process: the first is to ablate the carbon-metal mixture while the second breaks up the larger ablated particles in order for them to take part in the nanotube growth process. SWNTs condense from the vapourization plume and are collected outside the furnace. The yield of this technique has been improved by using rotating targets and continuous ablation and is able to produce up to gram quantities. By varying the temperature of the process, the diameter of the synthesized nanotubes can be controlled.

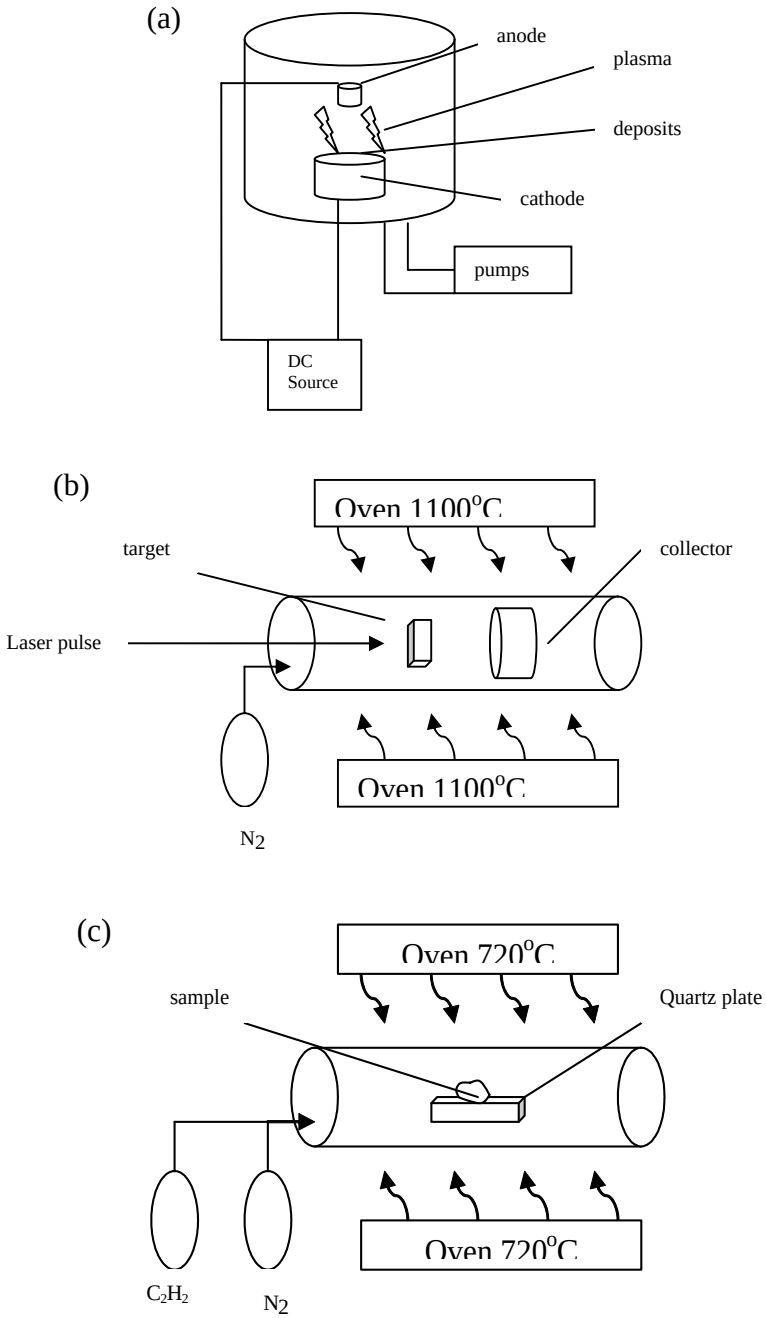

Fig. 1.2: Schematics of the different carbon nanotube growth methods and the TEM images of the carbon nanotubes grown by the respective methods. (a) arc discharge, (b) laser ablation, (c) catalytic deposition.

1.6.3 Catalytic Growth

The catalytic growth method essentially involves the decomposition of hydrocarbon gas in the presence of a transition metal catalyst in a chemical vapour deposition chamber. In 1993, this approach was used to grow MWNTs by the decomposition of acetylene over Fe particles at temperatures of about 600^0C-800^0C (22). A much higher temperature of ~1100^0C is required for the synthesis of SWNTs as they have a higher energy of formation. Due to the high temperature, carbon monoxide or methane is used as the carbon source as they are more stable than acetylene. The catalytic growth method is ideal for the growth of nanotube film on planar substrates such as silicon.

The catalytic growth method has garnered much attention because of several advantages that the method has over other synthesis processes (8). Firstly, the process produces very few or no codepositied carbon allotropes, thus eliminating the need for further purification process. Secondly, since catalytic growth method allows the synthesis of nanotubes directly on substrates, lithographic methods can be used to pattern the catalyst on these planar substrates, thereby allowing for patterned or selective area growth. By controlling the size of the pores of the catalyst, one is also able to control the diameter of the synthesized carbon nanotubes.

1.7 Growth Mechanisms

Studies of catalyst grown multiwalled carbon nanotubes indicate that growth occurs through precipitation of dissolved carbon from a moving catalytic particle surface (23). Growth terminates when the catalyst particle is deactivated or when stable metal

carbide is formed. It is energetically favourable for the surface of the newly formed fibre to precipitate as low energy basal planes of graphite; hence the nanotubes form in tubular morphology. However, due to the curvature of the graphite layers, an additional elastic energy term is introduced into the free energy equation of nucleation and growth. As a result, a lower limit to the diameter of the carbon fibres that can from curved graphite layers is installed. The implication of this is that in order for us to explain the growth of carbon nanotubes, new mechanisms must be thought of.

The growth of MWNTs and SWNTs might occur via two different mechanisms. Open MWNTs are seldom observed in samples grown via the arc method. During nucleation, all the growing layers of the tube remain open during growth. A layer undergoes closure because of pentagonal rings formed due to disturbances or perturbations during the growth process or due to stability considerations between structures with hexagonal and pentagonal morphology. Hence, open-ended tubes are improbable since the dangling bonds at the ends would cause a large increase in the energy of the system. This energy is minimized through interactions between adjacent layers. Bonds present between layers are dynamic, and incorporation of carbon species during growth occurs through continuous breaking and reforming of the lip around the fringe of an open-ended tube.

A mechanism suggested for SWNT growth involves the role of a catalyst during growth. Catalyst atoms decorate the dangling bonds of the open end of a tube and achieve growth by a ‘scooter’ mechanism. The catalyst atoms ‘scoots’ around the rim of the open tube and absorb incoming carbon atoms, causing the tube to grow. However, through theoretical calculations, it is shown that SWNTs will have a strong tendency to form

close ends by forming pentagons and ejecting any catalyst atoms. Until now, however, there is no consensus as to which is the dominant mechanism that governs the growth of SWNTs (24).

1.8 Applications of Carbon Nanotubes

Since their discovery, researchers around the world have tried to utilise the unique electronic structure, mechanical strength, flexibility and dimensions of carbon nanotubes for a wide range of applications. Most of these applications apply to both SWNTs and MWNTs, although electronic applications based on SWNTs show more success.

1.8.1 Nano-electronic Devices

Carbon nanotubes are viewed as ideal 1-D nanostructures, hence they show great promise as quantum wires and in tiny electronic devices. The Delft group built the first single molecule field-effect transistor, using individual semiconducting SWNTs (25). The transistor is made of a nanotube connecting two metal electrodes and operates at room temperature. The band structure for this device is similar to that of two Schottky-type diodes connected back to back and its performance is comparable in switching speeds to existing devices. The next crucial step in this application would be to integrate the device into circuits. However, existing technology in nanotube fabrication does not allow the construction of the complex device architecture that the industry needs today. The only solution is to have self-assembly of the carbon nanotubes in the desired architecture. This has to be realized first before nanotubes electronics can become a practical reality.

1.8.2 Nanoscale Junctions

There is the possibility of joining nanotubes of different helicity, which would lead to the fabrication of heterojunction devices (26). MWNTs have been studied and there are observations of varying changes in electronic properties along the length of the tubes. Junction devices can be designed from two nanotube segments, one of which is semiconducting and another that is metallic in nature through doping with impurities such as boron. As such, a whole new branch of nanoscale physics is beginning to develop. Predictions and theoretical models have already paved the way for this field to advance.

1.8.3 Nanoprobes

A novel use of nanotubes is as nanoprobes for such as tips of a scanning probe microscope (27). This application makes use of the nanotubes' high aspect ratio, mechanical strength and elasticity. A successful demonstration is the use of a nanotube tip on an atomic force microscope that was used to image the topography of TiN-coated aluminium film. A bundle of MWNTs is first attached to the cantilever using adhesive bonding. The free end of the bundle is then sheared to form the 'sharp' tip. Owing to its flexibility, nanotube tips do not crash as readily as the conventional tips. Also, the dimension of the nanotube tip makes it particularly suitable to image deep features like cracks. As nanotubes are conducting, they can be used as tips for the scanning tunnelling microscope. This seems a really promising application of carbon nanotubes; however, the vibration of individual freestanding tips can disrupt some of the advantages brought by the small tube dimensions, especially during high-resolution imaging.

1.8.4 Nanotube Electrodes

The potential of nanotubes playing the roles of electrodes is also being hotly researched, particularly due to the fact that carbon based electrodes have been used for decades in important electrode applications such as fuel cells and batteries. Initial studies using MWNT electrodes in bioelectrochemical reactions showed high reversibility and catalytic activity at the nanotube electrodes (25). Nanotubes can catalyse oxygen reduction reactions, where the electron transfer rates are much higher than those observed on other carbon-based electrodes. As oxygen is an important reaction in fuel cells, this clearly shows the potential of nanotubes serving as electrodes in such devices.

1.8 Optical Limiting Effects of Carbon Nanotubes

Carbon nanotubes also show excellent optical limiting characteristics. This was first reported with experimental evidence by P. Chen *et al* in 1999 (28). This discovery opened a whole new field of applications for carbon nanotubes. This property can be applied to photonic devices, such as optical switches and optical communications. However, much of the research done up till then on the electronic and optical properties of carbon nanotubes have been theoretical predictions instead of actual experimental measurements. Here I shall discuss the optical limiting property of carbon nanotubes based on the work done in that landmark paper.

The carbon nanotubes are dissolved in a suitable solvent such as ethanol. Laser pulses of wavelengths 532nm and 1064nm are used. It is observed that at incident fluences lower than 0.06 J/cm, energy transmittance is a constant. At higher fluence energies, energy transmittance decreases with increasing incident fluence, exhibiting

optical limiting property. The experiment is repeated for 1064nm wavelength laser pulses and a similar trend is observed. This confirms carbon nanotubes as possessing broadband optical limiting qualities (28).

The same experiment is also repeated for C_{60} and carbon black, where the concentration is normalized for easy comparison. The limiting threshold, which is defined as the incident fluence at which transmittance falls to that of linear transmittance, is around 1.0 J/cm^2 for carbon nanotubes, lower than C_{60} and carbon black at 532nm. At 1064nm, limiting phenomenon totally vanishes for C_{60}, while carbon black has a much higher limiting threshold.

In C_{60}, the dominant mechanism to explain the optical limiting property is excited state absorption. Ground-state absorption promotes electrons into excited states. There is no ground-state absorption at 1064nm, hence there is no optical limiting observed in that wavelength.

For carbon nanotubes, ground-state absorption is absent in both 532nm and 1064nm. From the electronic structure study of carbon nanotubes, carbon nanotubes have a lower work function, lower binding energy and stronger plasma excitation. This, coupled with the fact that carbon nanotubes show broadband limiting response, suggests that the limiting property results from a different mechanism, nonlinear scattering. Coincidentally, this mechanism is determined to be the dominant process for carbon black suspensions.

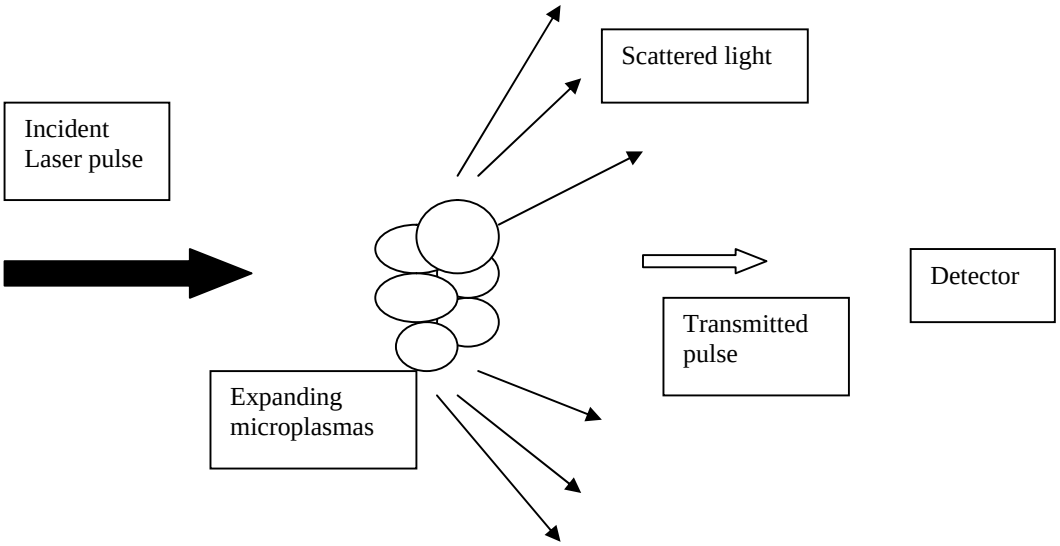

Fig 1.3: Schematic of Non-linear Scattering Process

During nonlinear scattering, heating of the carbon nanotubes by the laser pulses lead to vaporisation and ionisation of carbon particles, and then the formation of rapidly expanding microplasmas. These microplasmas strongly scatter light in the transmitted beam direction, thereby leading to a decrease in the transmitted light direction. At the same time, the nanotubes conduct heat to the surrounding liquid, leading to the generation of solvent microbubble growth, which also plays a part in decreasing the measured transmitted light.

1.9 Carbon Nanotubes as Field Emitters

With conventional cathode ray tubes gradually being replaced by flat panel displays, there is a great interest in electron field emitters. This can be credited to the recent development of cheap and robust field emitting materials. One such material is the carbon nanotube.

1.9.1 What is Field Emission?

Field emission is the process whereby electrons are emitted under high field conditions from the surface of a solid by tunnelling through the surface potential barrier (29). As shown in Fig1.4, The potential barrier is square-shaped when no electric field is applied. When a potential is applied, the surface potential barrier becomes triangular. The amplitude of local field F just above the surface of the solid determines the gradient of the slope. The local field F is given by

$$F = \frac{V\beta}{d_0} \tag{4}$$

where V is the applied voltage, d_0 the distance between the two parallel electrodes, and ß is the field enhancement factor. Field emission peaks at the Fermi level; hence, field emission is determined by the workfunction ϕ. The Fowler-Nordheim model describes the dependence the emitted current on the local field and workfunction as

$$I \propto \left(F^2/\phi\right)\exp\left(-B\phi^{3/2}/F\right) \tag{5}$$

where B = 6.83 X 10^9 (V $eV^{-3/2}$ m^{-1}). From the relationship, we can see that the emitted current is strongly affected by factors such as variations in the shape of emitter and the chemical state of the solid or its surface. When the field emission follows the Fowler-

Nordheim model, one can determine either ϕ or ß from the slope of the Fowler-Nordheim plot, which is determined by plotting $\ln\left(I/V^2\right)$ against $1/V$.

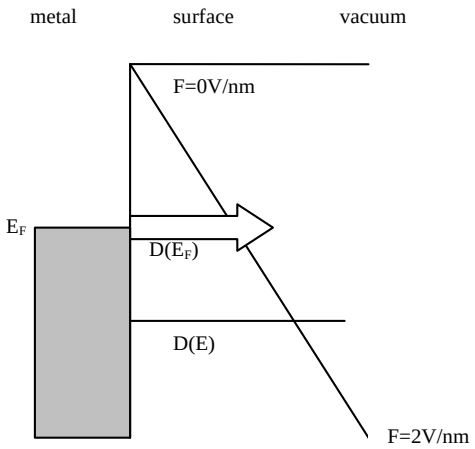

Fig. 1.4: Field emission model from a metal emitter (29).

Field emitters are preferred over thermoelectric emitters because of several advantages (29). Firstly, field emitters do not need be heated, hence there is no need for the installation of a heater in the device. Secondly, the electrons emitted by field emitters have a smaller energy spread. Thirdly, field emitters are easily synthesized in microscopic or nanoscale dimensions and can be made into arrays. Lastly, the emitter current is easily controlled by applied voltage.

1.9.2 Why Carbon Nanotubes?

Carbon nanotubes are viewed as one of the most exciting materials for a field emitter cathode, one of the key discoveries that will spearhead field emission displays to the top of the flat panel display market. There are several reasons for this:

- High aspect ratio
- High mechanical strength
- Conductive
- Low turn-on fields
- High current densities
- Easy to fabricate

1.10 Aim of Project

As discussed in the sections before, owing to their wide range of excellent properties, carbon nanotubes are being earmarked for a variety of applications, two of which are as optical limiting materials and field emission cathodes. In this project, we attempt to modify MWNTs in a bid to enhance their original properties.

The first part of the project attempts to enhance MWNTs as optical limiters by coating a layer of a-Ag or a-Au. Au and Ag nanoparticles are known to possess large nonlinear optical properties and ultrafast time response and their optical properties were also actively studied by picosecond and femtosecond laser in the surface plasmon absorption region. Hence, we attempt to combine MWNTs with Au and Ag to form new composite materials with optical limiting properties that exceed that of pure nanotubes.

The second part of the project investigates carbon nanotubes as field emitters. There has been much research on improving the field emission properties of carbon nanotubes, such as chemical doping and structural modifications. Here, we modify the carbon nanotubes via Ar and N_2 plasma etching, before measuring their respective field emission characteristics. We characterize the modified MWNTs in comparison to the parent MWNTs using various techniques such as SEM, UPS, XPS and Raman spectroscopy.

Chapter 1

References:

(1) Saito, R., Dresselhaus, G. and Dresselhaus, M. S., Physical Properties of Carbon Nanotubes, London: Imperial College Press, 1998. Chap. 1.

(2) Kroto, H. W. *et al.*, *Nature* (London) **318**, 162 (1985).

(3) Ijima, S., *Nature* (London), **354**, 56 (1991).

(4) Kelly, B. T, Physics of Graphite, London: Applied Science, 1981.

(5) Field, J. E., Properties of Diamond, London: Academic Press, 1979.

(6) Kroto, H. W., *Nature* (London), **329**, 529 (1987).

(7) Yakabson, B. I. and Smalley, R. E., *Am. Sci.*, July-August, **324** (1997).

(8) Bonard, J-M., *et al.*, *Solid State Electronics*, **45,** 893 (2001).

(9) Saito, R., *et al.*, *Appl. Phys. Lett.*, **60**, 2204 (1992).

(10) Dresselhaus, M. S., *Electronic Properties of Carbon Nanotubes and Applicatios*, Carbon Filaments and Nanotubes: Common Origins, Differing Applications?, Bir?, L. P., *et al.* ed., London: Kluwer Academic Publishers, 2001.

(11) Zhang, X. F., *et al.*, *J. Cryst. Growth.*, **130**, 3 (1993).

(12) Ijima, S., *et al.*, *Nature*, **356**, 777 (1992).

(13) Chico, L., *et al.*, *Phys. Rev. Lett.*, **76**, 971 (1996).

(14) Hamada, N., *et al.*, *Phys. Rev. Lett.*, **68**, 1579 (1992).

(15) Dresselhaus, M. S., *et al.*, Science of Fullerenes and Carbon Nanotubes, New York: Academic Press, 1996.

(16) Odom, T. W., *et al.*, *Nature*, **391**, 62 (1998).

(17) Wildoer, J. W. G., *et al.*, *Nature*, **391**, 59 (1998).

(18) Tans, S. J., *et al.*, *Nature*, **386**, 474 (1997).

(19) Thrower, P. A., *Carbon*, **37**, 1677 (1999).

(20) Journet, C., *Appl. Phys. A*, **67**, 1 (1998).

(21) Thess, A. *et al.*, *Science*, **273**, 483 (1996).

(22) Jose-Yacaman, M., *et al.*, *Appl. Phys. Lett.*, **62**, 657 (1993).

(23) Oberlin, A., *et al.*, *J. Cryst. Growth*, **32**, 335 (1976).

(24) Ajayan, P. M., *Carbon Nanotubes*, Nanostructured Materials and Nanotechnology, ed. Nalwa, H. S., Academic Press (London) 2002.

(25) Tans, S. J., *et al*., *Nature*, **386**, 464 (1997).

(26) Dresselhaus, M. S., *et al.*, *Phys. World*, January, 33 (1998).

(27) Dai, H. J., *et al.*, *Nature*, **384**, 147 (1996).

(28) Chen, P., *et al.*, *Phys. Rev. Lett.*, **82**, 2548 (1999).

(29) Bonard, J-M., *et al.*, *Carbon*, **40,** 1715 (2002).

Chapter 2: Experimental Techniques

In this chapter, I shall introduce the various experimental techniques and characterization methods that were used in both projects and provide a brief overview of their principles.

2.1 Synthesis Techniques

2.1.1 Sputter Deposition of Catalyst

Sputtering is a process whereby material is dislodged and ejected from the surface of a solid or liquid due to the momentum exchange during surface bombardment by energetic colliding particles. Coating of any material can be done easily since the coating material is passed into the vapour phase in a physical process rather than chemical or thermal process. Sputtering methods are favoured in thin film synthesis because of the following reasons:

1) High deposition rate
2) Able to deposit and maintain stoichiometry of the target
3) Uniform deposition on large wafers
4) High reproducibility of films
5) Good adhesion to the substrate

Fe is deposited on Si (100) substrate using the Denton radio frequency magnetron sputtering machine. The target is placed onto the cathode in the vacuum chamber together with the substrates, which are placed onto the rotating substrate plate. The chamber is first evacuated to pressures around 10^{-6} to 10^{-7} Torr. Argon is then introduced into the chamber to serve as the bombarding species at a working pressure of 10mTorr. A radio

frequency of 13.56MHz is applied to produce the Ar plasma. The benefit of using a radio frequency field is that the electrons are oscillating, hence no accumulation of electrons occur at the target even if an insulator is used. During deposition, the charged Ar ions diffuse into the Crookes dark zone, acquiring almost all of its energy from the voltage drop before hitting the target surface. The sputtered atoms leave the target surface with kinetic energies that range between 3-10eV. As they travel downwards under the electric field, they undergo collisions with the sputtering gas atoms, thereby dissipating energy. The ejected atoms then condense onto the substrate to form a thin layer of film. In order to increase the uniformity of the deposited film, the substrate plate is rotated during deposition. Deposition rate is typically in the range of 5-50nm/min, depending on the power used during the process.

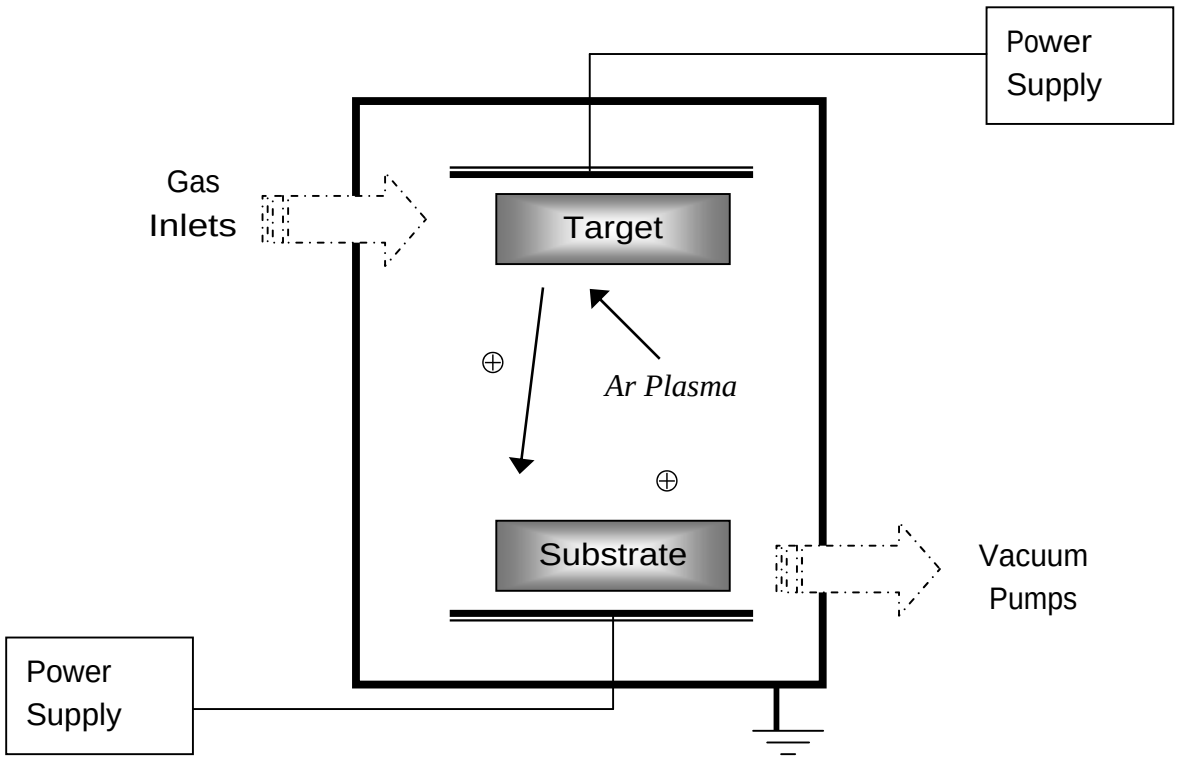

Fig 2.1: Schematic diagram of sputtering process.

2.1.2 Chemical Vapour Deposition

In this project, we employ the plasma enhanced chemical vapour deposition to synthesize our MWNTs. Chemical vapour deposition essentially takes place through the reaction between vapour phase reactants and the substrate to form a non-volatile solid film on the substrate. The process can be broken down into the following four steps (1):

1) Transportation of reactant gases species to the surface of the substrate.
2) Reactant species undergoes chemisorptions on the substrate surface.
3) Heterogeneous reaction between surface particles and absorbed reactant particles.
4) Desorption of reaction particles into the gaseous phase from substrate surface.

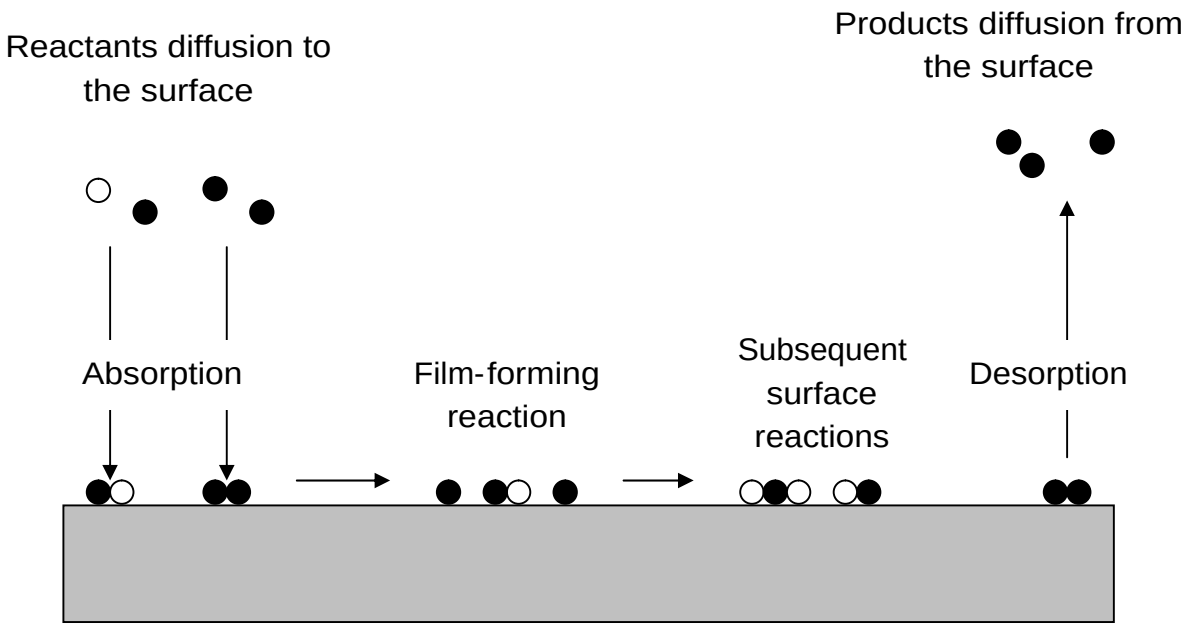

Fig 2.2: Schematic of the reaction processes in PECVD.

Two types of reactions may take place during deposition: heterogeneous reactions and homogeneous reactions. Heterogeneous reactions are the desirable reactions since they only occur on the heated surface, unlike homogeneous reactions, which are reactions that

take place in the gaseous phase. Homogeneous reactions result in the formation of gaseous clusters of the depositing material, resulting in the deposition of poorly adhering films. Controlling the process variables allows us to determine which type of reaction dominates.

We use catalytic chemical vapour deposition under plasma enhancement to synthesize our carbon nanotubes. The system is a Plasma Quest series III PQM-9157-A modified with a heating filament. Acetylene is decomposed in the presence of hydrogen to synthesise the MWNTs. The radio frequency biased showerhead, which also serves as the gas injector, can reach a maximum power of 550W at 13.56MHz and process pressures of up to 2Torr. The purpose of the radio frequency power is to produce the glow discharge that aids in the transfer of energy to the reactant gas by breaking the gas down.

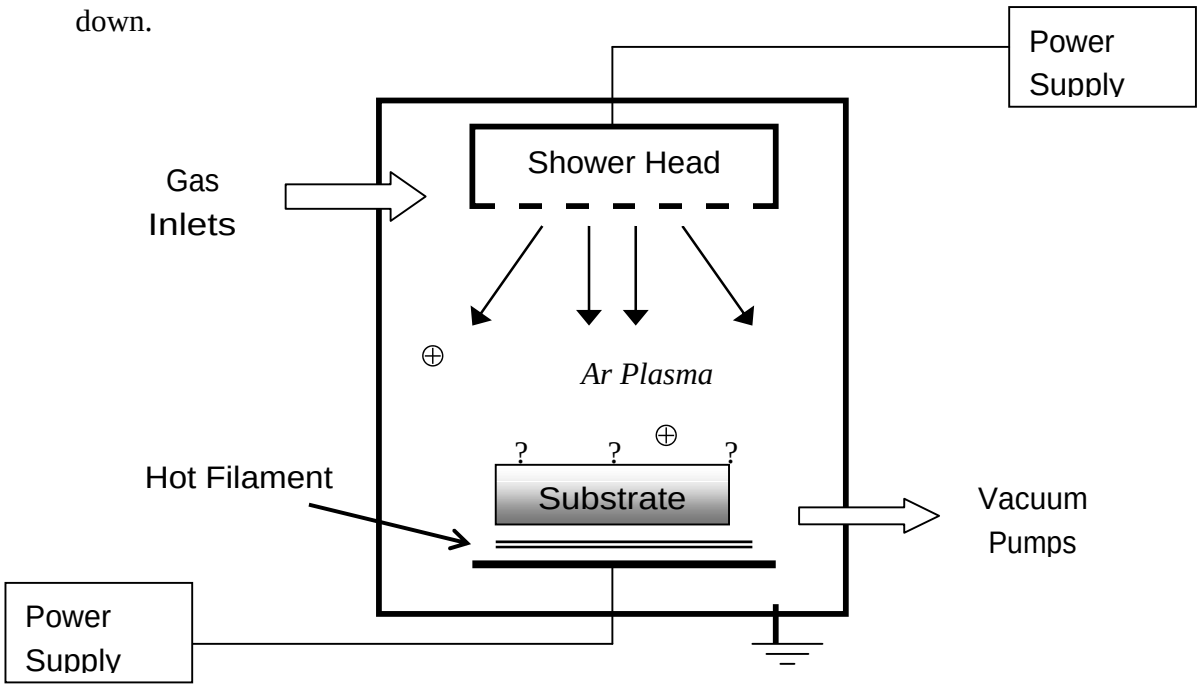

Fig 2.3: Schematic of Hot Filament PEVCD system.

The PECVD is first pumped down to a pressure of 10^{-6}Torr before the heating filament is turned on and heated up. After the desired process temperature is attained, acetylene is introduced into the chamber together with hydrogen or ammonia. Once steady state is achieved, the radio frequency power is turned on to produce the plasma. The free electrons formed by the plasma in the discharge region gain energy and collide with the reactant molecules, thereby causing ionisation. The reactant species then adsorb onto the catalyst surface and nanotube growth takes place. The rate of deposition is determined by the substrate temperature, deposits with less trapped by-products formed at higher temperatures. The various factors that have to be considered for the PECVD process include control and optimisation of radio frequency power, gas composition, flow rate of gaseous reactants, deposition temperature and total working pressure.

2.1.3 Electron Beam Evaporator

We used an electron beam evaporation system to coat our MWNTs with a-Au or a-Ag. This is a thermal process that uses a finely focused electron beam to hit the target material, which is held in a water-cooled crucible. The intense heat generated causes the target to evaporate and condense onto the MWNT film placed above the target. Approximately 5nm layer of a-Au or a-Ag was coated onto the MWNTs using the Univex 300 electron beam evaporator system

2.2 Characterization and Measurement Techniques

2.2.1 Scanning Electron Microscope

The scanning electron microscope (SEM) employs a finely focused electron beam to scans the sample surface in a raster pattern. The electrons that are incident on the sample originate can originate from a variety of sources, which determines the type of SEM. In thermionic emission SEM, the electrons are produced from a heated filament. Electrons in cold-field emission SEMs are extracted at room temperature, while the thermally assisted field SEM combines both.

The electron beam is travels down the column of the microscope and undergoes a multi-step demagnification with electromagnetic condenser lenses. When the beam finally reaches the sample surface, the beam diameter can range from 1μm to 1nm. The beam scans across the surface of the sample with the help of electromagnetic defection coils. Secondary electrons are released from the surface of the sample, which is collected to provide the image of the sample. Each signal is the result of some particular interaction between incident electrons and the specimen, which serve to provide different information about the specimen. These signals include secondary electrons, backscattered electrons, Auger electrons and X-rays. They are released when the incident electrons lose energy to the sample, in the process exciting various secondary emissions from the material. A scintillation material that produces light flashes detects the secondary electrons. These light flashes are detected and amplified by a photomultiplier tube. Proper adjustment of the accelerating voltage, beam current and spot diameter is required for optimisation. The SEM used in this research is the JOEL JSM 6700F, at 5kV operating voltage.

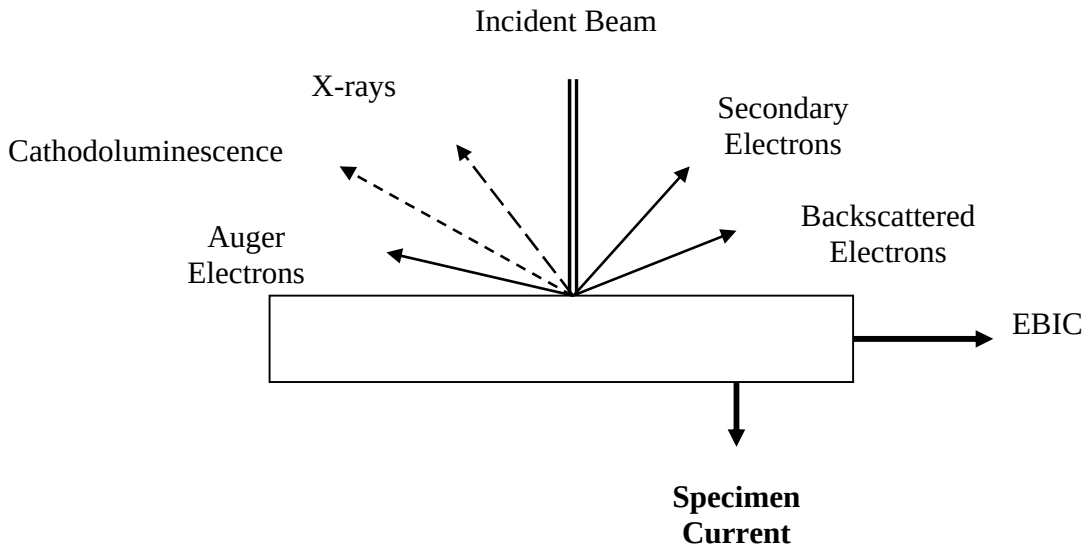

Fig. 2.4: Signals utilised in SEM for imaging and gathering of information of sample

2.2.2 Transmission Electron Microscopy

In transmission electron microscopy (TEM), the sample is irradiated with a high energy, highly coherent electron beam. Electrons are transmitted through the sample and an image is formed via an electron optic system. The optic system can also work in the diffraction mode, which allows a diffraction pattern of the crystalline sample to be seen. A real space image can be obtained from a diffraction spot by adjusting the bias on the electron optic lenses.

There are also two modes of imaging: dark field mode and bright field mode (2). In the bright field mode, the specular transmission beam is used. In this mode, normally perfect crystalline parts appear bright in the image while defects appear relatively dark. In the dark field mode, the defects, which are strong scatters of electrons, appear bright, making this mode useful for locating domains of a particular crystalline orientation.

TEM is a very sensitive process that can achieve atomic resolution (2). Hence, sample preparation is very important in order to obtain a high quality image. Samples must be very thin, of about a few hundred nanometers thick for sufficient transmittance.

Thick samples are usually thinned by mechanical polishing and then ion milling. TEM is a very useful tool in film growth characterization as it allows the imaging of growth interfaces. In recent years, in-situ TEM analysis techniques have been developed that allow the dynamic and kinetic processes of nanostructure synthesis to be observed.

2.2.3 Raman Spectroscopy

The working principle of Raman spectroscopy is based on the in elastic scattering of light by matter. We can see this effect through the energy diagram below (Fig. 2.5), which shows a molecular system with two vibrational energy levels separated by energy $h\nu_M$ (3). When a photon of energy $h\nu_L$ induces transitions to the virtual levels as shown, the transition back to ground state can take place in three pathways. When the transition starts and ends at the same vibrational levels, then it results in Rayleigh scattering. When the transitions end at a higher or lower energy level, then we have Stokes and anti-Stokes Raman scattering. Stokes Raman scattering is usually more intense than anti-Stokes Raman scattering as most molecules are initially at their ground state vibrational energies. Thus, we usually study the Stokes Raman spectrum.

In this project, we utilise a Renishaw Raman Scope 2000 System that has an attached Olympus microscope. The excitation source used was the 514nm line of an argon-ion laser.

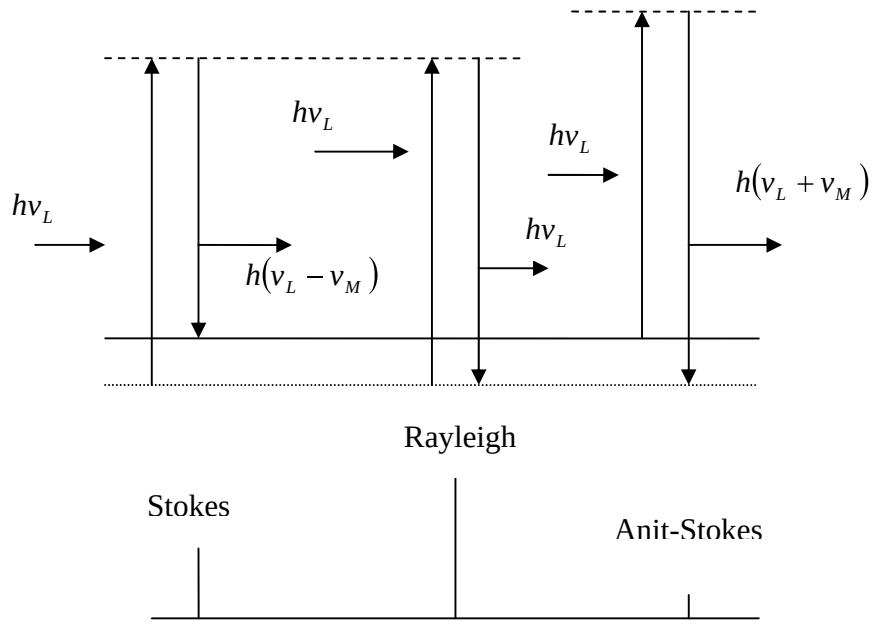

Fig. 2.5: Diagram of the energy level transitions involved in Raman scattering.

2.2.4 Synchrotron Light Source

The Singapore Synchrotron Light Source (SSLS) is used in this project, taking advantage of monochromatic, tuneable and highly coherent radiation source (4). Both X-ray photoelectron spectroscopy and valence band photoemission spectroscopy is done with the aid of the synchrotron radiation.

The SSLS consists of a compact superconducting storage ring with 700MeV electron energy and a bending field of 4.5T to produce the synchrotron radiation. The characteristic photon energy and wavelength is 1.47keV and 0.845nm, while the useful spectrum ranges from 10keV right down to the far infrared range, with the flux being a maximum in the soft X-ray region. At the other end of the spectrum, in the far infrared range, the edge effect is used to provide a high flux and brilliance throughout the whole

infrared range. There are several beamlines functioning at the time of writing and we performed our experiments the SINS beamline for our project.

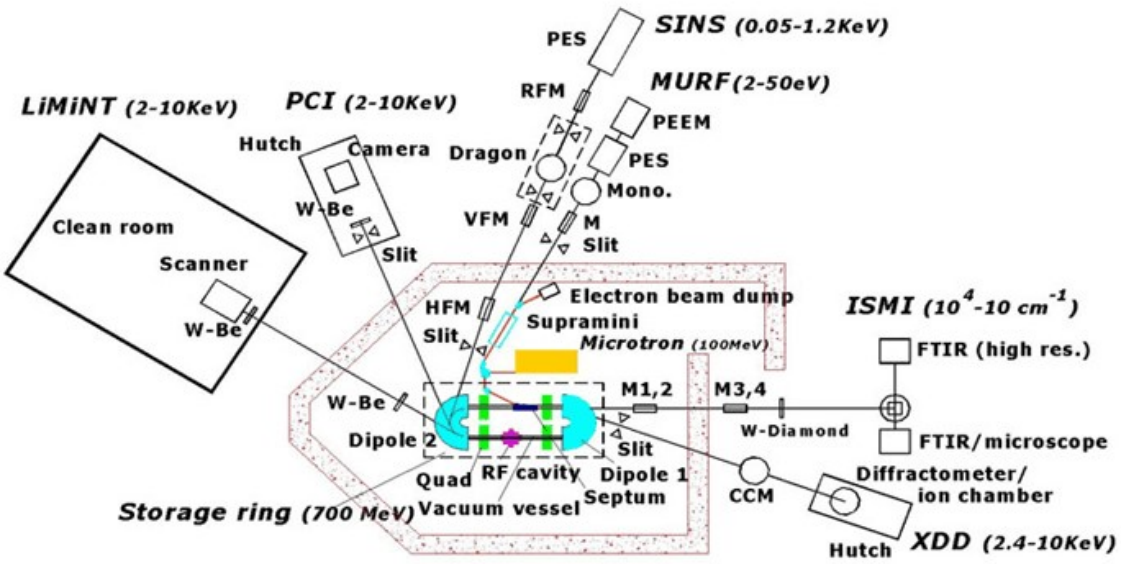

Fig. 2.6: Schematic diagram of the synchrotron system with its working beamlines (4).

2.2.5 Photoelectron Spectroscopy

Photoelectron spectroscopy (PES) is the study of the energies of photoelectrons emitted by incident radiation from sample surface. Kinetic energy of emitted electrons range from 0eV to the energy of the incident radiation.

Valence band PES allows the characterization of the Fermi level by the onset of the photoelectron emission. The spectrum can also trace out the density of states at the surface, thereby providing a picture of the band structure. We can also use the width *W* to obtain the workfunction of the sample given by:

$$\phi = h\nu - W \qquad (6)$$

2.2.6 X-ray Photoelectron Spectroscopy

X-ray photoelectron spectroscopy (XPS), or ESCA (Electron Spectroscopy for Chemical Analysis), uses soft X-rays as the primary particles. The technique involves the measurement of the kinetic energies of the emitted electrons due to interaction with incident soft X-rays.

The two sources generally used in XPS are Mg $K_{a1/2}$ or Al $K_{a1/2}$ (5). The primary X-ray photon creates a core energy level photoelectron upon absorption. This excitation then undergoes relaxation via two different pathways. In the first scenario, a secondary photoelectron is emitted when a valence band electron fills the hole at the core energy level. The second scenario involves the formation of a tertiary electron, Auger electron, after de-excitation. All elements with Z = 3 can be detected. Elements with lower Z cannot be detected since there are no core shells to excite (5).

Sometimes, when the sample under study is a semiconductor or insulator, the sample surface may become positively charged due to photoelectron emission and loss of electrons. This makes the emission of further electrons more difficult and results in an upward shift in the binding energy. This may be compensated for by a charge compensation device, which provides low energy electrons to the sample to compensate for the positive charge build-up. Negative charging may also occur due to excessive adsorption of negatively charged particles, though this rarely happens. This can be compensated for by low positive energy ion beam bombardment. The number of detected photoelectrons at a given energy gives the intensity in the XPS spectrum.

2.2.7 Optical Limiting Measurements

Fluence-dependent transmission measurement is used to study the optical limiting behaviour of the material. The sample is suspended in a suitable solution and placed in an optical cell in an optics set-up. Laser pulses of a certain wavelength are then passed through the sample, and a detector records the transmittance of the laser pulses by the sample. The reduction in the laser pulse intensity after passing the sample reflects its optical limiting property.

The laser pulse is produced by the Nd:YAG laser. A Q-switch is used to control the rate of laser pulse emission. Pulses can be fired in a continuous mode or as single shots. The emitted pulse is guided by a series of reflective mirrors and focused on to a crystalline polarizer P1 by a focusing mirror (Fig 2.7). The plane-polarized laser pulse is then passed through a waveplate-polarizer combination that serves as an energy modifier.

Upon exiting the energy controller, the laser pulse is passed through a second crystalline polarizer so as to maintain the plane of polarization. The pulse is then focused onto an aperture. The aperture serves to collimate the pulse into a Gaussian form, thereby improving the quality of the pulse. The laser pulse is then incident on a beam-splitter. The beam-splitter, as its name suggests, ‘splits’ the pulse into two. One of the split pulses is passed directly to and recorded by the detector, serving as the reference signal. The second split pulse is focused onto the optical cell containing the suspended sample. Upon passing through the sample, the laser pulse transmitted by the sample in the cell. This transmitted signal is then recorded by the detector. A ratio of the transmitted signal to the reference signal is then calculated.

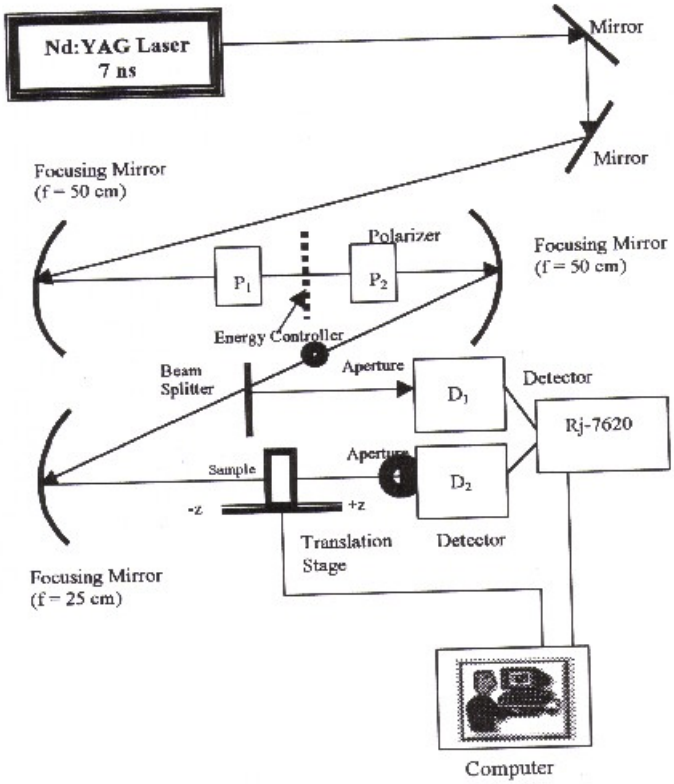

Fig. 2.7: Schematic of optical limiting experiment set-up.

The set-up can be used for different wavelengths, such as 532nm and 1064nm, depending on the requirement of the experiment. The intensities of the laser pulse emitted can also be varied by using filters that are placed at the output of the Nd:YAG laser. The filters serve to reduce the transmitted laser pulse energy. This allows a wider range of laser energy to be incident on the sample, allowing the investigation of the optical limiting property of the sample at low energies.

2.2.8 Field Emission Measurements

Fig2.8: Photograph of the field emission measurement setup. The homemade chamber is seen on the left side of the picture while the computer and audio-visual linkup is shown on the right.

The field emission measurements in this project were carried out in a 'home-made' field emission measurement system (Fig. 2.8). The steel chamber wall, which is cut out from a single steel block, has seven ports, one of which has a high electrical feed through. Two pins of the four-pin feed through is connected to the high voltage power supply that is used apply a potential difference across the cathode and the anode. The chamber is pumped down to ~10^{-7}Torr before taking measurements. One of the ports of

the steel chamber is converted into a liquid nitrogen cold finger to aid in maintaining the low pressure. Maintenance of this low pressure is crucial as the field emission properties of materials are affected due to charging effect at higher operating pressures and also to prevent contamination. There is a microscope and a CCD camera installed above the top viewing port that allows the capture of any field emission patterns observed.

Chapter 2

Reference:

1) Veprek, S., *Thin Solid Films*, **130,** 135 (1985).

2) PC 5215, Physics of Nanostructures, Lecture Notes, National University of Singapore.

3) Wartewig, S., IR and Raman Spectroscopy, Weinheim:Wiley-VCH, 2003, pp. 31-33.

4) Singapore Synchrotron Light Source Website, *http://ssls.nus.edu.sg*

5) Mathieu, H. J., *Elemental Analysis by AES, XPS and SIMS*, Non-destructive Elemental Analysis, Alfassi, Z. B. Ed., London: Blackwell, 2001, Chap.6.

Chapter 3: Optical Limiting Properties of a-Au and a-Ag Coated Carbon Nanotubes

In this chapter, I shall present the optical limiting characteristics of a-Au or a-Ag coated MWNTs and compare them with that of pure MWNTs. A mechanism is proposed for the observed experimental results.

3.1 Introduction

Owing to their excellent optical limiting properties, carbon nanotubes have emerged as front-runners of next-generation optical limiters (1). However, the search for even better optical limiters for use in the protection of sensors from intense laser pulses has motivated many researchers to investigate new composite nanomaterials, in the hope of discovering superior optical limiting properties. Jin et al. started by attaching polymers on MWNTs, but the results showed no improvement in optical limiting properties (2).

Noble metal colloids or nanoparticles such as Au and Ag nanoparticles have been known to possess large nonlinear optical properties and ultrafast time response. Their optical properties were also actively studied by picosecond and femtosecond laser in the surface plasmon absorption (SPA) region. In this project, we investigate the optical limiting performances of carbon nanotubes incorporated with a-Au and a-Ag particles, respectively.

3.2 Surface Plasmon Absorption in Au and Ag Nanoparticles

One of the unique features of noble metal nanoparticles is the strong colour of their colloidal solution, which is a direct result of surface plasmon absorption (2). The

origin of the surface plasmon absorption band is the electromagnetic field-induced collective oscillation of free connduction electrons occupying states near the Fermi level in the conduction band. Particle size effects on this plasmon band have been studied by Mie and Maxwell-Garnett theory (3, 4), which has predicted that the plasmon absorption peak red-shifts and the band broadens with increasing nanoparticle size, and this has been confirmed experimentally. It is interesting to note that this surface plasmon band is actually sensitive to excitation by lasers, hence making them useful for nonlinear optical applications. Hence, much investigation has been carried out to understand the nature of this surface plasmon absorption effect (2).

Basically, a laser pulse with the right intensity and wavelength can cause interband or intraband electron transitions in a metal nanoparticle (2). The excited electrons become free carriers of a wide range of kinetic and potential energies. The potential energies are associated with the unoccupied and occupied states in the conduction band. This process results in a reduction in intensity of the ground-state plasmon band, but also produces a transient absorption spectrum that is significantly broadened due to free carrier absorption. The excited electrons will interact with each other to form an “internally thermalized distribution”. The electrons also lose energy by thermalizing externally with the lattice via electron-phonon interactions. This leads to a substantial recovery of the bleached ground-state plasmon absorption band. All these processes take place within a few picoseconds from the point of laser excitation.

However, there is further delay to the complete recovery of the ground-state plasmon band due to the phonon-phonon relaxation processes that follow, whereby thermal energy is dumped into the solvent resulting in changes to the surrounding

medium. This can influence the plasmon resonance frequency of the nanoparticles. It has been reported by Kamat *et al* that this slow component takes ~90ps for 40-60nm silver colloids (5). Ahmadi *et al* reports that the lattice phonon lifetime in 15nm gold nanoparticles is greater than 50ps (6). As such, the total relaxation time for the ground-state plasmon band is within 100ps. The optical limiting characteristics of Au and Ag nanoparticles have been widely researched upon in various systems and show promising results (7-8). Hence, there is ultrafast response from these noble metal nanoparticles that make them potential broadband, ultrafast optical limiters and also as fast optical switches.

3.3 Experimental Procedure

3.3.1 Synthesis of Random Carbon Nanotubes

A layer of Fe catalyst is first deposited onto Si (100), using radio frequency magnetron sputtering process at room temperature, at 50W radio frequency power and 5mTorr pressure. The deposition lasts 6mins, and occurs in the presence of Ar gas, which serves as the plasma. The target used is a Fe foil of 0.5mm thickness and 99.99% purity. The Fe on Si (100) sample (henceforth Fe/Si) is then placed into the hot filament plasma enhanced chemical vapour deposition (HFPECVD) system for carbon nanotube synthesis. The heating filament is made of an alloy comprising Fe, Ni and Cr. The Fe/Si substrate is placed directly on the heating coil to ensure that the temperature of the substrate and the coil is the same. This is essential because the process temperature measured by Al-Cr junction thermocouple is that of the heating coil, since the thermocouple is in direct contact with the coil.

The synthesis is carried out via the decomposition of acetylene in the presence of hydrogen. The first step of the synthesis process involves treating the substrate with hydrogen plasma at 630℃ and RF power of 100W. This temperature of corresponds to passing about 8A of current through the coil. At this temperature, the oxide desorbs from the catalyst surface, which helps in the formation of catalytic particles by making the catalyst grains more defined. The entire hydrogen etching process takes 600s. The second step involves introducing acetylene and hydrogen into the system at flow rates of 15sccm and 60sccm respectively. The substrate temperature is kept at 630℃ with temperature fluctuations of ±20℃. The deposition process takes about 180s. A field emission scanning electron microscope (FE-SEM), operated at 5 kV accelerating voltage was used to characterize the coated MWNTs. The thickness of the MWNTs grown is ~20nm.

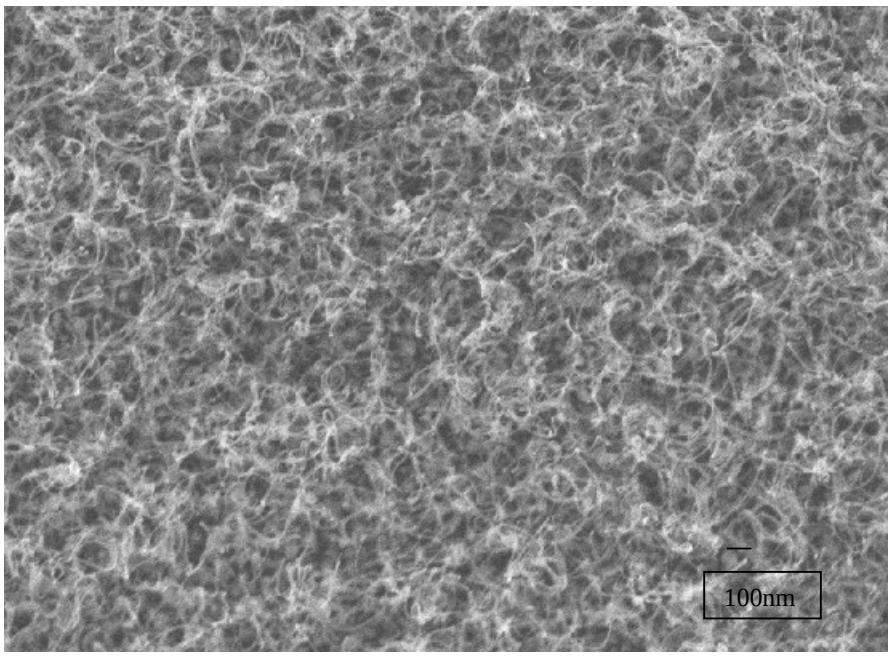

Fig. 3.1: SEM image of random MWNTs synthesized using HFPECVD.

3.3.2 Why Random MWNTs?

We choose to synthesize randomly oriented MWNTs rather than well-aligned MWNTs to facilitate the lengthwise coating of the MWNTs with a-Au and a-Ag nanoparticles. Previous work from our group has demonstrated that attempts to coat well-aligned MWNTs with a-SiC and a-SiN resulted in only the formation of tubular structures on the tips of the MWNTs while the length of the nanotubes remaining bare.

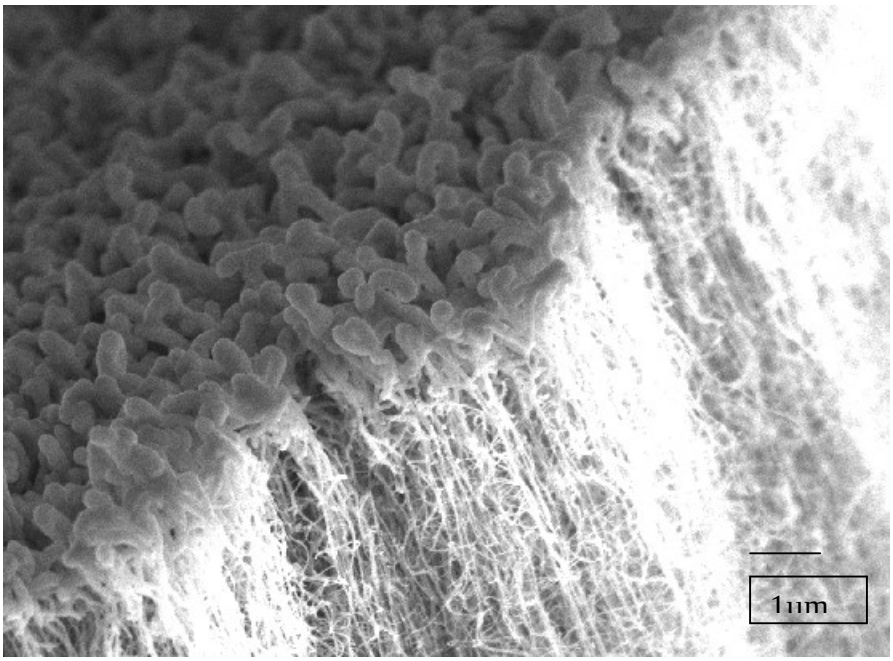

Fig. 3.2: SEM image of a-SiN deposited on well-aligned carbon nanotubes. SiN encapsulates the tip of the nanotubes, forming tubular structures.

This is essentially due to the high packing density of well-aligned MWNTs, which is a necessary condition for the nanotubes to be aligned. But the high density makes it difficult for the a-SiN and a-SiC molecules to permeate between the closely packed MWNTs for lengthwise deposition. Thus, in order to achieve a more uniform coating of a-Au and a-Ag nanoparticles on the MWNTs, we choose to synthesize

randomly oriented MWNTs, which are more sparsely packed, thereby allowing space for deposition along the nanotube length.

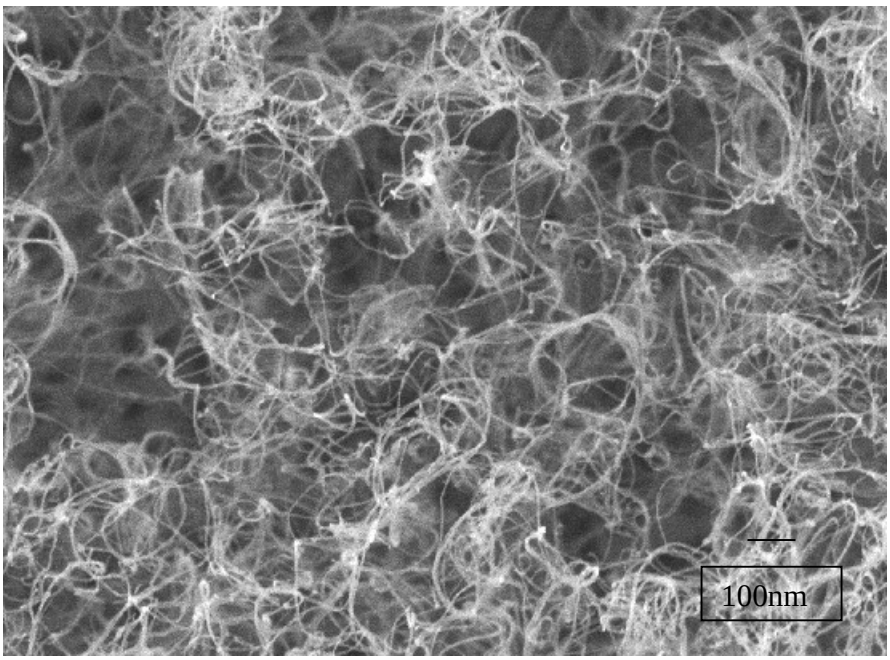

Fig. 3.3: Random MWNTs which are more widely spaced.

3.3.3 Coating of a-Au and a-Ag Nanoparticle Film

Au or Ag are coated on MWNTs by the vaporization of pure Au or Ag targets in a Leybold Univex 300 E-beam evaporator system, at a pressure of about 5 x 10^{-6} Torr. The vaporized Au and Ag condensed to form an amorphous film on the nanotube walls. Both coatings are controlled to be about 5 nm thick, achieving a total tube diameter of about 30 nm for each individual MWNT. The coated MWNTs are characterized by field emission SEM as before. It can be observed from the SEM images that the MWNTs are almost completely coated with a-Au or a-Ag nanoparticle films. The coatings are almost along the whole length and circumference of the MWNTs.

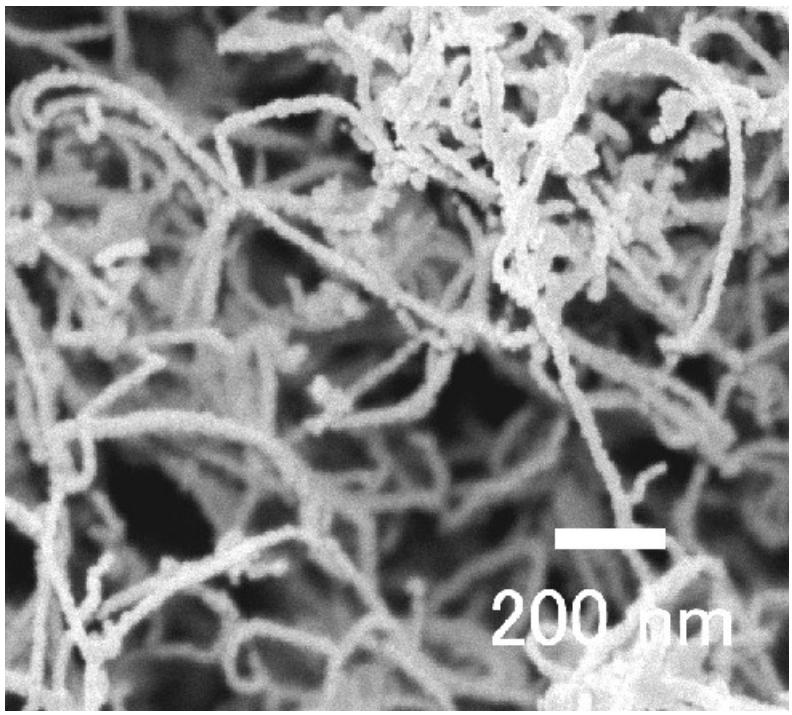

Fig 3.4: SEM image of MWNT coated with 5nm of a-Au (MWNT-Au05).

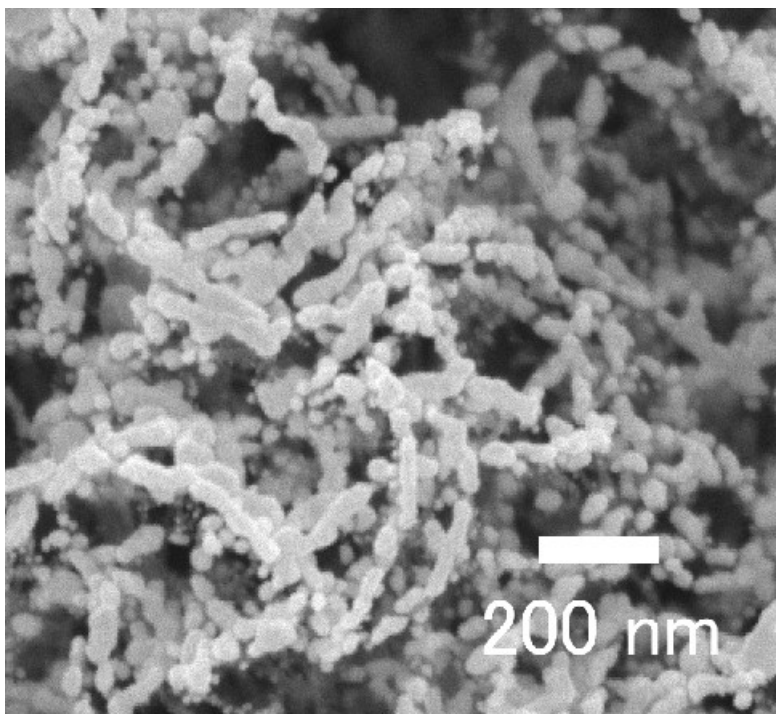

Fig 3.5: SEM image of MWNT coated with 5nm of a-Ag (MWNT-Ag05).

3.3.4 Optical Limiting Measurements

To prepare the samples for optical limiting measurements, the coated MWNTs are put into distilled water and sonicated for a few minutes. The concentration of each sample is adjusted to give a linear transmission of 70 % at 532 nm and 1064 nm. Optical limiting measurements are investigated by fluence-dependent transmittance measurements using linearly polarized nanosecond optical pulses from a Q-switched, Nd:YAG laser with pulse duration of 7 ns and beam waist of about 40 μm at the focal point. The set-up of the experiment is as discussed in Chapter 2. Each data in this experiment is collected using a single shot mode with a time interval of 10 seconds. A computer-controlled Shimadzu UV2101 spectrophotometer is used to record the absorption spectra for all the samples in the 300 – 1100 nm wavelength region.

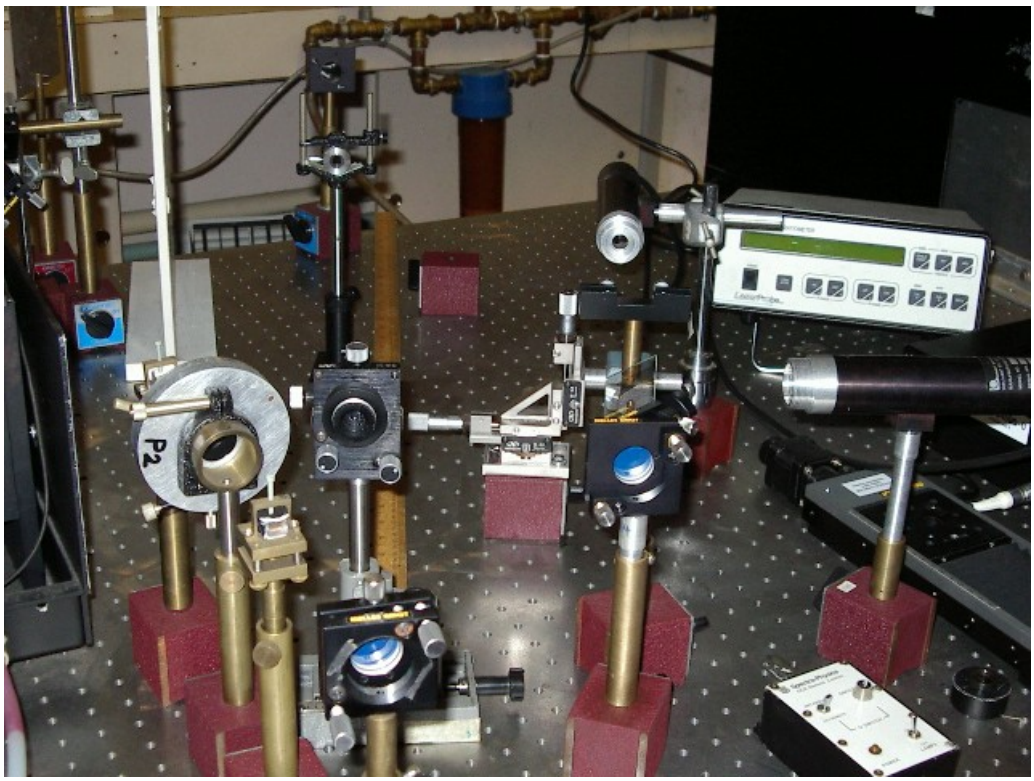

Fig. 3.6: Optical limiting experiment set-up.

SEM images of MWNT-Au05 (Fig. 3.7) after sonication are also taken to ensure the coating remained on the nanotubes. A drop of distilled water containing the coated nanotubes is placed onto a Si substrate and dried in air for a day before transferring to the SEM for characterization. It is noticed that significant amounts of coating still remained on the nanotubes. However, about 30% of the coating had been removed during the destructive sonication process. The peeling off of Au and Ag particles from MWNTs is probably due to the large vibrational forces present during the sonication process. This observation is not surprising as early studies by Biercuk et al. (9) and Liu et al. (10) showed that strong sonication could even chop a nanotube into shorter pipes.

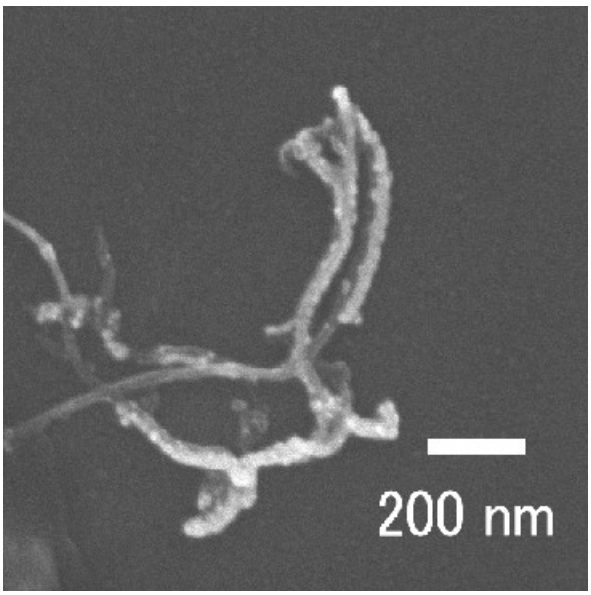

Fig. 3.7: SEM image of MWNT-Au05 after sonication.

3.4 Results and Discussion

The optical limiting properties of MWNT-Au05 and MWNT-Ag05 are measured at wavelengths of 532nm and 1064nm and compared with those of pure MWNT at the same concentration with 70% linear transmission. Measurement results at 532 nm and 1064 nm for MWNT, MWNT-Au05 and MWNT-Ag05 suspended in water at room temperature are shown in Fig. 3.8a and 3.8b.

We observe that at 532nm, the optical limiting characteristics of MWNT-Au05 and MWNT-Ag05 are superior compared to pure MWNTs. It seems that the coating of the a-Au and a-Ag nanoparticles on MWNT not only preserves the original optical limiting properties of the MWNT, but also enhances the overall characteristic. At low input fluences, the transmittance is independent of the input fluence and is almost constant. This trend continued until the onset of optical limiting which occurred at 0.2 J/cm^2 for MWNT-Au05 and MWNT-Ag05 while the onset of optical limiting for the pure MWNT occurred at 0.4 J/cm^2.

By increasing the input energy, near linear reduction of transmittance versus input fluence was observed. At 7 J/cm^2, the transmittance of MWNT-Au05 and MWNT-Ag05 dropped to about 0.3 while the transmittance of pure MWNT at this input fluence is about 0.4. Thus there is a clear enhancement in the optical limiting effect of MWNTs after coating with a layer of a-Au and a-Ag nanoparticles. However, optical limiting enhancement is not seen at 1064 nm wavelength (Fig. 3.8b) as all three samples show almost identical optical limiting characteristics at all input fluences.

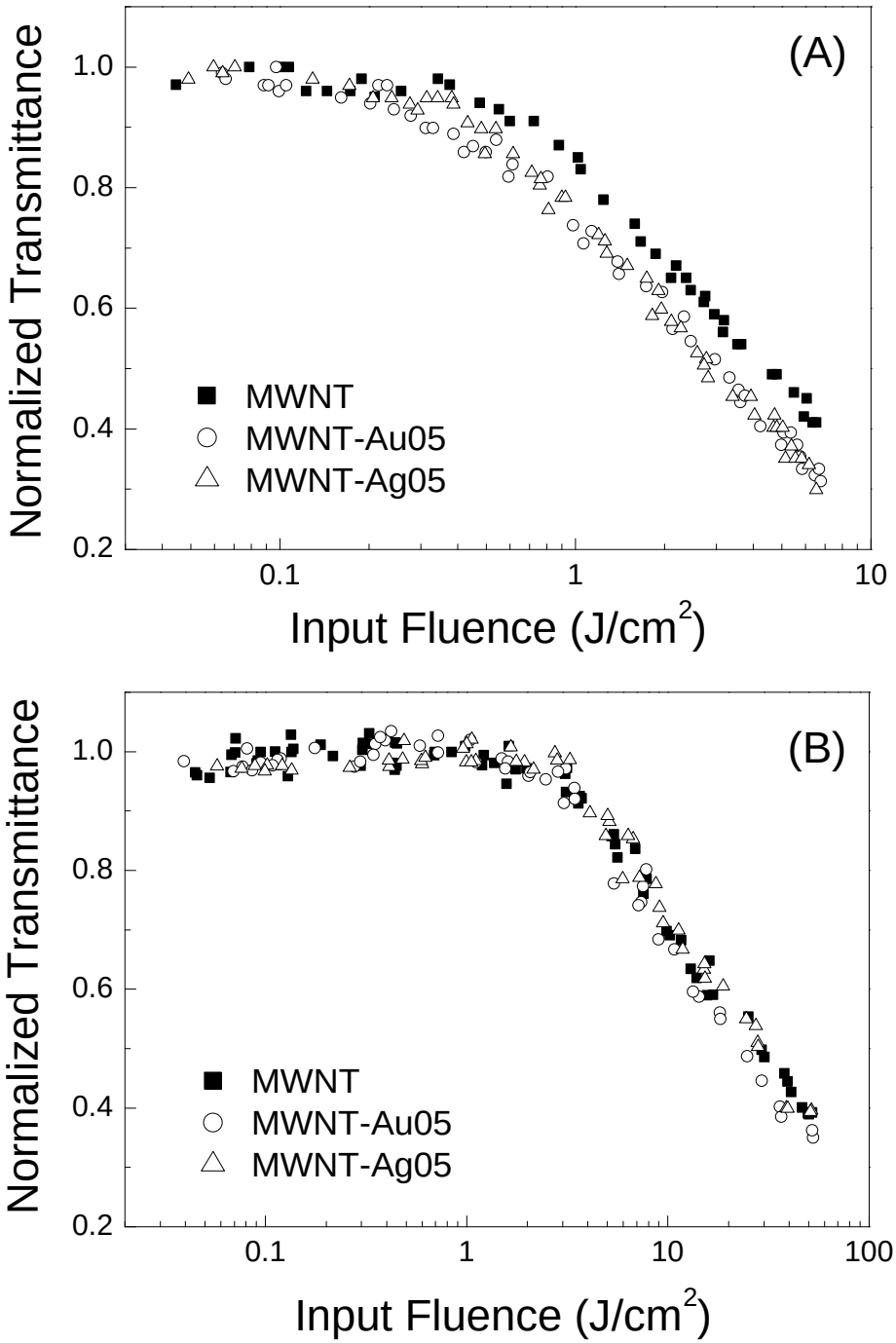

Fig. 3.8: Optical limiting behavior of MWNT, MWNT-Au05 and MWNT-Ag05 at (a) 532nm and (b) 1064nm.

In Fig 3.9, we present the UV-visible absorption spectra for MWNT, MWNT-Au05 and MWNT-Ag05. It can be seen that there is a surface plasmon peak in the absorption spectra for both MWNT-Au05 and MWNT-Ag05. For MWNT-Au05, there is a resonant peak in the region of 520 nm; while for MWNT-Ag05, the resonant peak occurs in the region of 420 nm. These two peaks are attributed to the surface plasmon absorption effects of the a-Au and a-Ag nanoparticles on the MWNTs. The relative low and broad peaks can be explained by the wide size distribution of the nanoparticles.

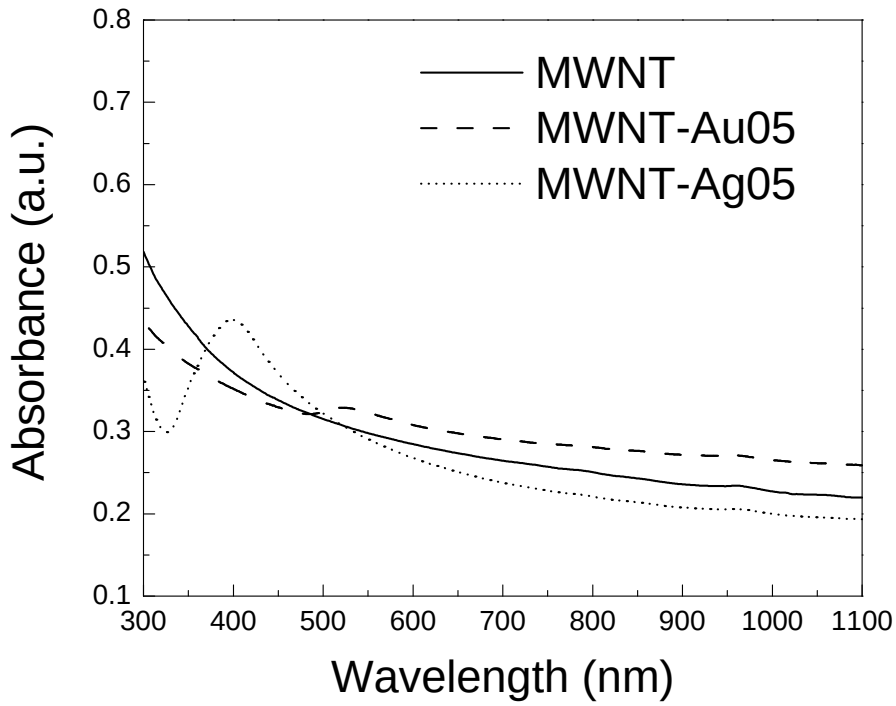

Fig. 3.9: UV-visible absorption spectra for MWNT, MWNT-Au05 and MWNT-Ag05 at room temperature. Surface plasmon resonance peaks are observed at 520 nm for MWNT-Au05 and 420 nm for MWNT-Ag05.

As observed from the experimental results, coating of MWNTs with a-Au and a-Ag nanoparticles does indeed improve their optical limiting properties. A proposed reason for the improvement is the contribution of the surface plasma absorption of a-Au and a-Ag nanoparticles on the MWNTs that causes an overall increase in the non-linear scattering effect.

The absorption band is due to the electromagnetic field-induced collective oscillations of the surface plasmons. The photon energy absorbed will cause expansion of the metal particles into a microplasma state within nanoseconds, thereby inducing a scattering center (8). It is also believed that the heat absorbed will be transferred to the surrounding water, which can lead to formation of microbubbles when approaching boiling temperatures (11). These microplasma and microbubbles perform the role of large light scattering centers around the metal particles, thus resulting in strong nonlinear scattering effect. Further evidence that surface plasma absorption is indeed responsible for the optical limiting enhancement is the result of the optical limiting measurements at 1064nm. From Fig. 3.8b, the measurements show that the coated MWNTs do not exhibit any obvious enhancement of optical limiting behavior compared to its parent MWNTs, The reason for this is that the laser pulse wavelength is far beyond the surface plasmon resonance range, hence no surface plasma absorption by the a-Au and a-Ag nanoparticles take place.

Although free-carrier absorption of a-Au and a-Ag particles as reported by R. Philip et al. should also be considered as a contributing factor leading to OL enhancement (12), we believe that the dominant mechanism still is the surface plasma absorption by the coated a-Au and a-Ag.

In order to obtain direct evidence of the superior nonlinear scattering effects due to the coated a-Au and a-Ag nanoparticles, we performed a nonlinear scattering measurement. The experiment involves measuring the energy dependence of the scattered light as a function of scattering angles at 532 nm. The experimental set-up is based on previous work (13). Measurements with positive angles from 10° to 80° at 4 different input energies (0.26 J/cm^2, 0.52 J/cm^2, 1.56 J/cm^2, 5.2 J/cm^2) are presented in Fig. 3.10. We detected almost identical scattered energies for all samples at low input fluences, 0.26 J/cm^2 and 0.52 J/cm^2. However, at 1.52 J/cm^2 and 5.2 J/cm^2 input fluences, the experiments clearly demonstrate that MWNT-Au05 and MWNT-Ag05 have superior scattering properties compared to its parent MWNTs at most angles. The enhancement can even be 1.4 times as high as that of pure MWNTs. This coincides with the fall in transmittance at high input fluences for optical limiting measurements. These observations clearly agree with our optical limiting results (Fig. 3.8a), whereby coated MWNTs show better optical limiting properties with increasing laser intensity.

Photostability of the samples is verified as the absorption spectra before and after optical limiting measurements show similar trends. This is further confirmed by repeated optical limitng measurements at 532 nm and 1064 nm, in which the same characteristics are observed. Previous work from our group also suggests that the optical limiting enhancement effect is material dependent (14). Coating amorphous SiC or Si_xN_y on MWNTs will not improve OL performance, as SiC and Si_xN_y are essentially not optically active and do not possess additional light-scattering effect.

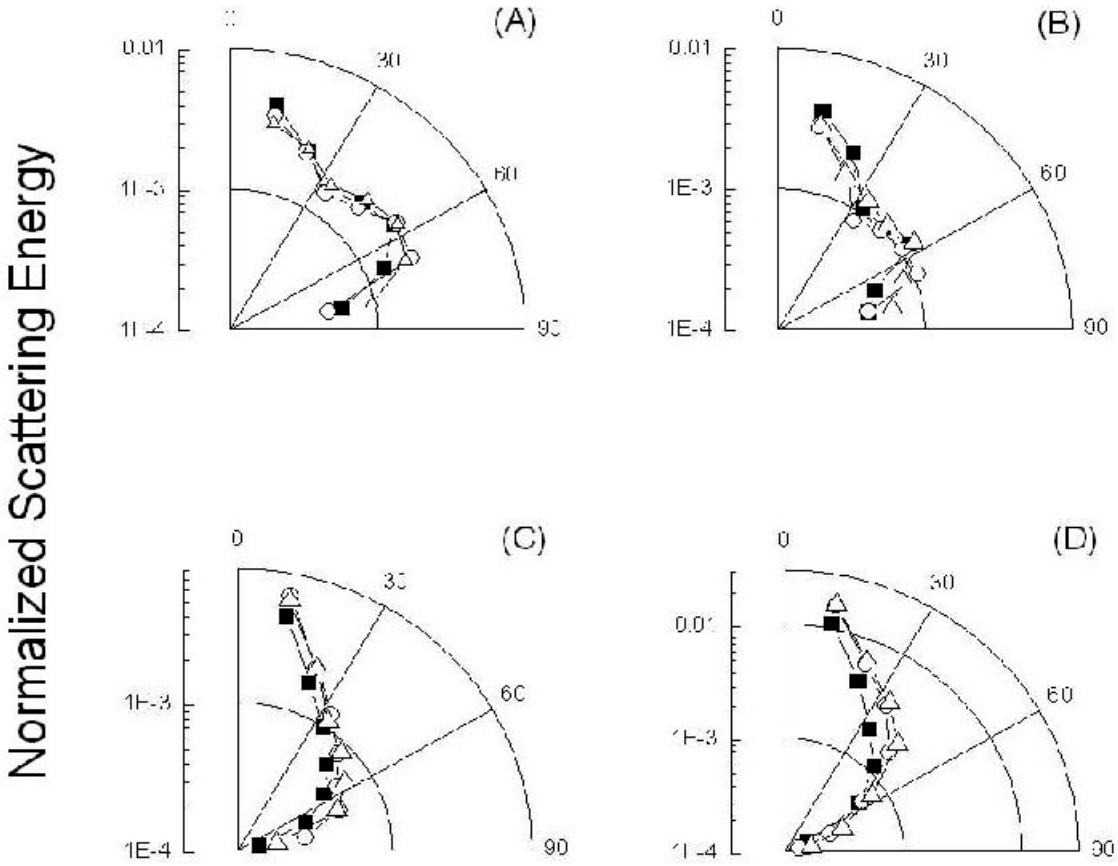

Fig. 3.10: Energy dependence of the scattered light as a function of scattering angles as measured with 532 nm, at 4 different input energies: (a) 0.26 J/cm^2; (b) 0.52 J/cm^2; (c) 1.56 J/cm^2 and (d) 5.2 J/cm^2. (■ MWNT, ○ MWNT-Au05, △ MWNT-Ag05, the Y-axis is normalized as 1 at 0°).

3.5 Conclusion

In this project, we have successfully synthesized a new class of nanomaterials, a-Au and a-Ag coated MWNTs, and investigated their optical limiting properties at 532nm and 1064nm wavelength using nanosecond laser pulses. Experimental results show that optical limiting behavior at 532 nm for the coated MWNTs is better than the parent MWNTs, which are already considered as benchmarks for high performance optical limiter. We believe that the improvement is due to increased nonlinear scattering arising from surface plasmon effects of Au and Ag nanoparticles. The fact that almost no optical limiting improvement is observed at 1064nm, since the wavelength is far beyond the surface plasmon resonance range, gave further confirmation to the validity of the proposed mechanism. Nonlinear scattering measurements were also conducted to show more directly the superior scattering properties of MWNT-Au05 and MWNT-Ag05 over pure MWNTs. Thus, by coating nanotubes with thin amorphous Au or Ag, we obtain a new composite material that gives better optical limiting effectiveness. Such materials show great promise as candidates for broadband optical limiters of various optical systems for eye and sensor protections due to their superior optical limiting performances.

Chapter 3

Reference:

1) Vivien, L., *et al.*, *Carbon*, **40**, 1789 (2002).

2) Philip, R., *et al.*, *Phys. Rev. B*¸ **62**, 19 (2000).

3) Kreker, M., The Scattering of Light and Other Electromagnetic Radiation, New York: Academic, 1969.

4) Mie, G., *Ann. Phys.*, **25**, 377 (1908).

5) Kamat, P. V., *et al.*, *J. Phys. Chem. B,* **102**, 3123 (1998).

6) Ahmadi, T. S., *et al.*, *J. Phys. Chem.*, **100**, 8053 (1996).

7) Sun, Y.P., *et al*., *J. Phys. Chem.*, **103**, 77 (1999).

8) Francois, L., *et al.*, *J. Phys. Chem. B*, **104**, 6133 (2000).

9) Biercuk, M. J., *et al*. *Appl. Phys. Lett*., **80**, 2767 (2002).

10) Liu, J., *et al.*, *Science*, **280**, 5367 (1998).

11) Ispasoiu, R. G., *et al.*, *J. Am. Chem. Soc.*, **122**, 11005 (2000).

12) Philip, R., *et al.*, *Phys. Rev. B*, **62**, 13160 (2000).

13) Sun, X., *et al*., *Appl. Opt.*, **39**, 1998 (2000).

14) Chin, K. C., *et al.*, *Chem. Phys. Lett.* **383**, 72 (2004).

Chapter 4: Field Emission Properties of Plasma Etched MWNTs

In this part of the project, we modify MWNTs by treating them with Ar and N_2 plasma in a bid to enhance the field emission characteristics of MWNTs. We measure the field emission using a custom designed vacuum chamber and characterize the modified MWNTs so as to ascertain the changes that have occurred due to the etching treatment.

4.1 Introduction

One of the most exciting applications for carbon nanotubes is in field emission displays. Early into its discovery, the potential of carbon nanotubes as excellent field emitters were evident as articles reported extremely low-turn on fields and high current densities in 1995. Moreover, with the development of the catalytic chemical vapour deposition method, controlled deposition of carbon nanotubes can take place via catalyst patterning. The breakthrough for this technology came in 1998 when a crude display using nanotubes as emitters was first presented to the world (1).

4.2 Experiment Details

4.2.1 Experimental Procedure

For our field emission measurements, we synthesized random MWNTs on Fe/Si substrates. The synthesis recipe is as discussed in Chapter 3. It is important that the substrate is Si as it is conductive, thereby facilitating the field emission measurements process. The field emission characteristic of pure MWNTs is measured first as the control experiment. We then place the MWNT film on Fe/Si back into the Denton radio

frequency magnetron sputtering machine for plasma etching using N_2. The etching is carried out at 100W power and 2mTorr pressure.

After etching, we measure the field emission characteristics before etching the same set of samples for a further ten minutes. The field emission measurements are then repeated. Hence, we obtain the field emission characteristics of pure MWNTs, as well as that after 10min and 20min of plasma etching (samples labelled CNT-N10min and CNT-N20min respectively). The whole process is then repeated on a fresh set of MWNTs using Ar as the etching agent (CNT-Ar10min and CNT-Ar20min). The plasma-etched MWNTs are imaged using SEM as before.

4.2.2 Field Emission Set-up

The field emission set-up is shown in Fig. 4.1. The anode to cathode distance is fixed at 150μm, which is the thickness of the microglass spacer used to isolate the cathode from the anode. The height of the random MWNT is negligible compared to the thickness of the spacer. The role of the cathode is performed by the MWNT film on the Fe/Si substrate, while the anode is a commercially available ITO glass slide.

The voltage applied across the anode and cathode is provided by a Kiethley 237 high voltage power source. The field emission measurement process is controlled by the computer interface using a Labview program that communicates with the voltage supply through an IEEE connection. Hence, the voltage can be increased at any desired step and interval. The applied voltage during the field emission measurement was kept to a maximum of 450V(3V/μm), and increased in 5V steps at 1s intervals.

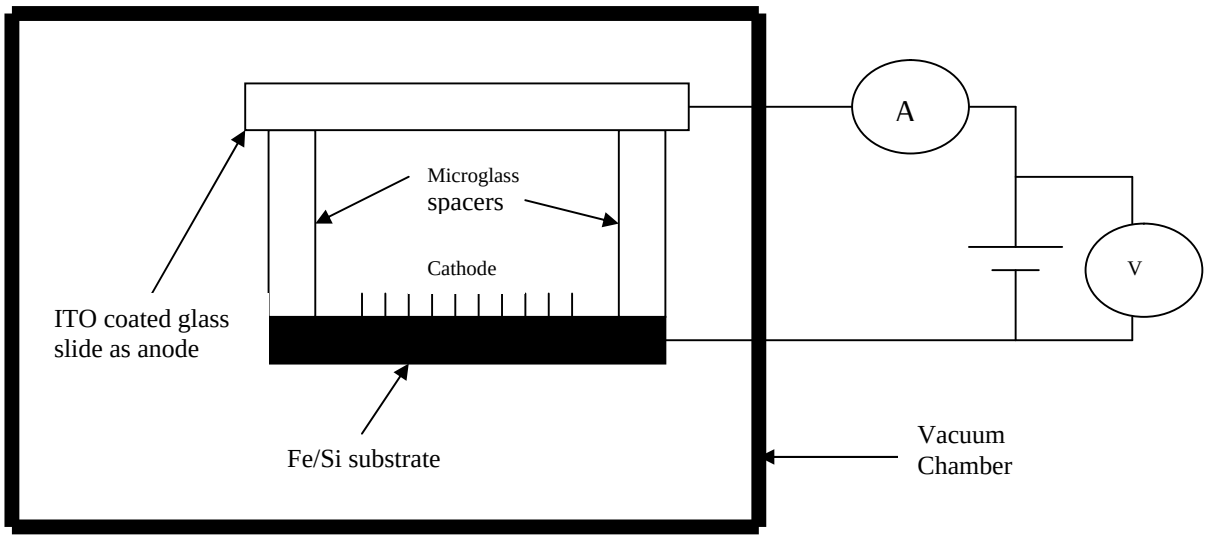

Fig. 4.1: Schematic of Field Emission Set-up

4.3 Experimental Results

The MWNTs that we synthesized in this project are similar to the one shown in Fig. 3.1 and 3.3. Figs. 4.2 to 4.5 show a series of SEM images of the random MWNTs after 10min and 20min N_2 and Ar plasma treatment respectively.

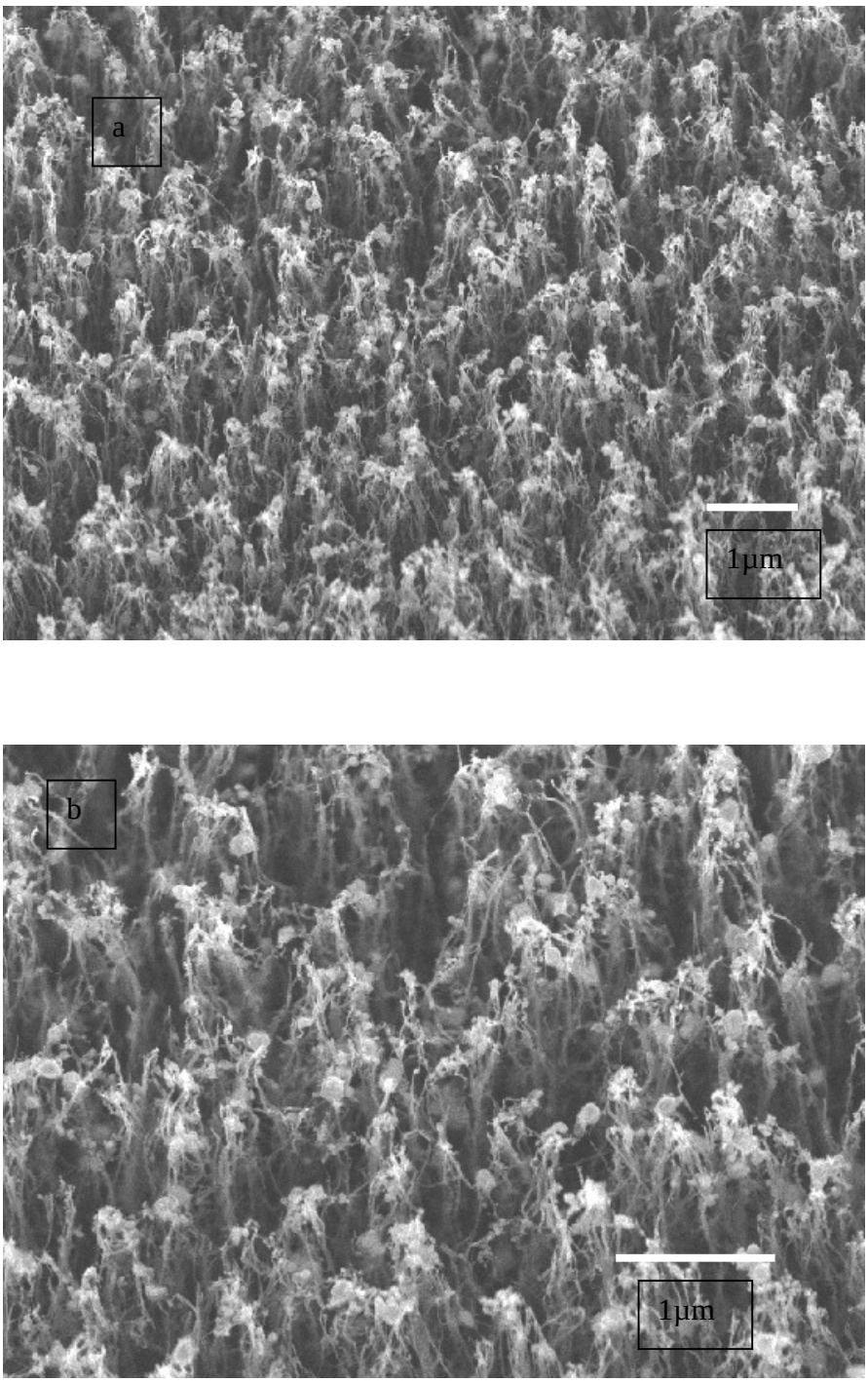

Fig. 4.2(a): SEM image of random MWNT after 10min plasma treatment with N_2 (CNT-10min). (b): High magnification SEM of the same sample.

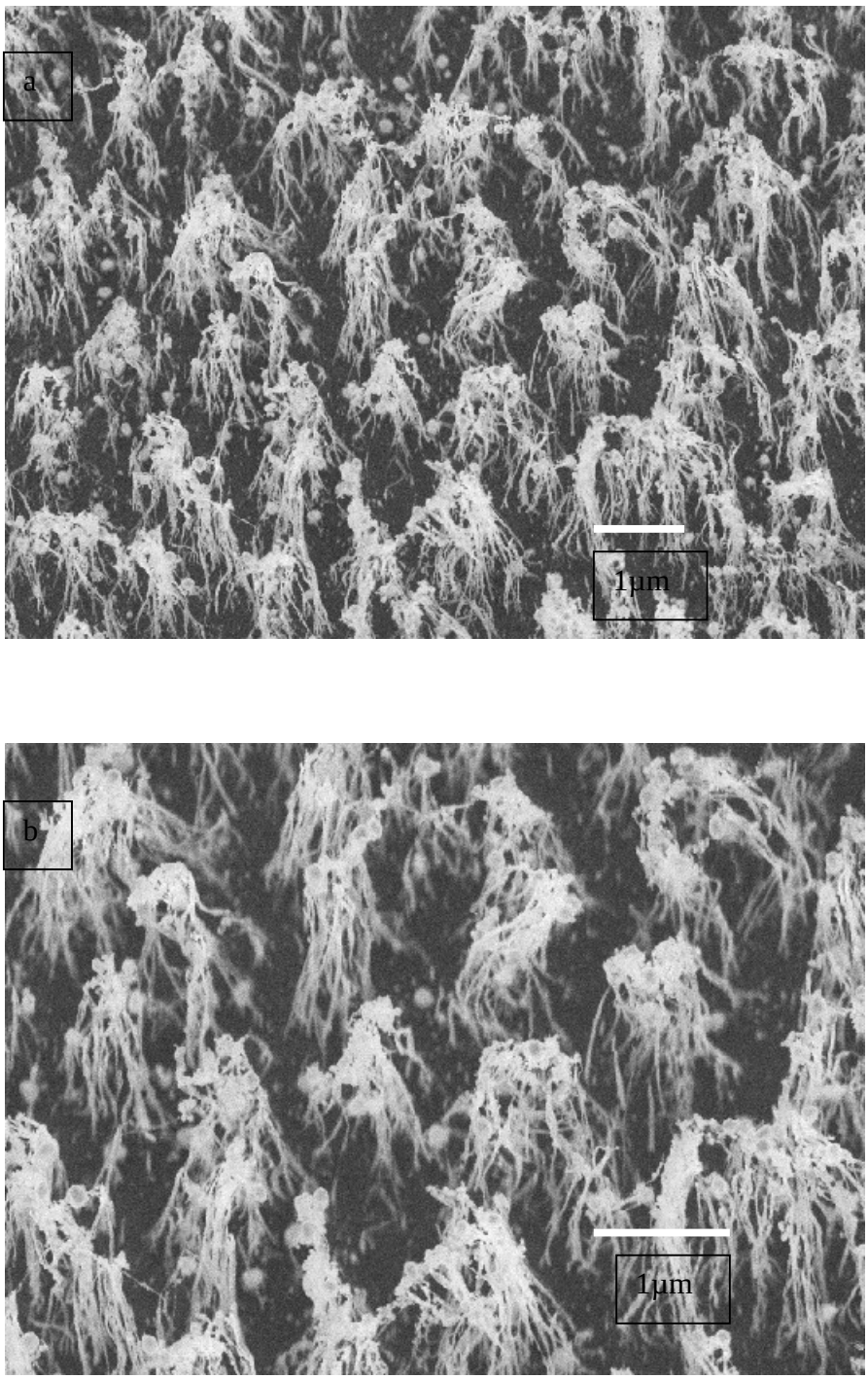

Fig. 4.3(a): SEM image of random MWNT after 20min plasma treatment with N_2 (CNT-N20min). (b): High magnification SEM of the same sample.

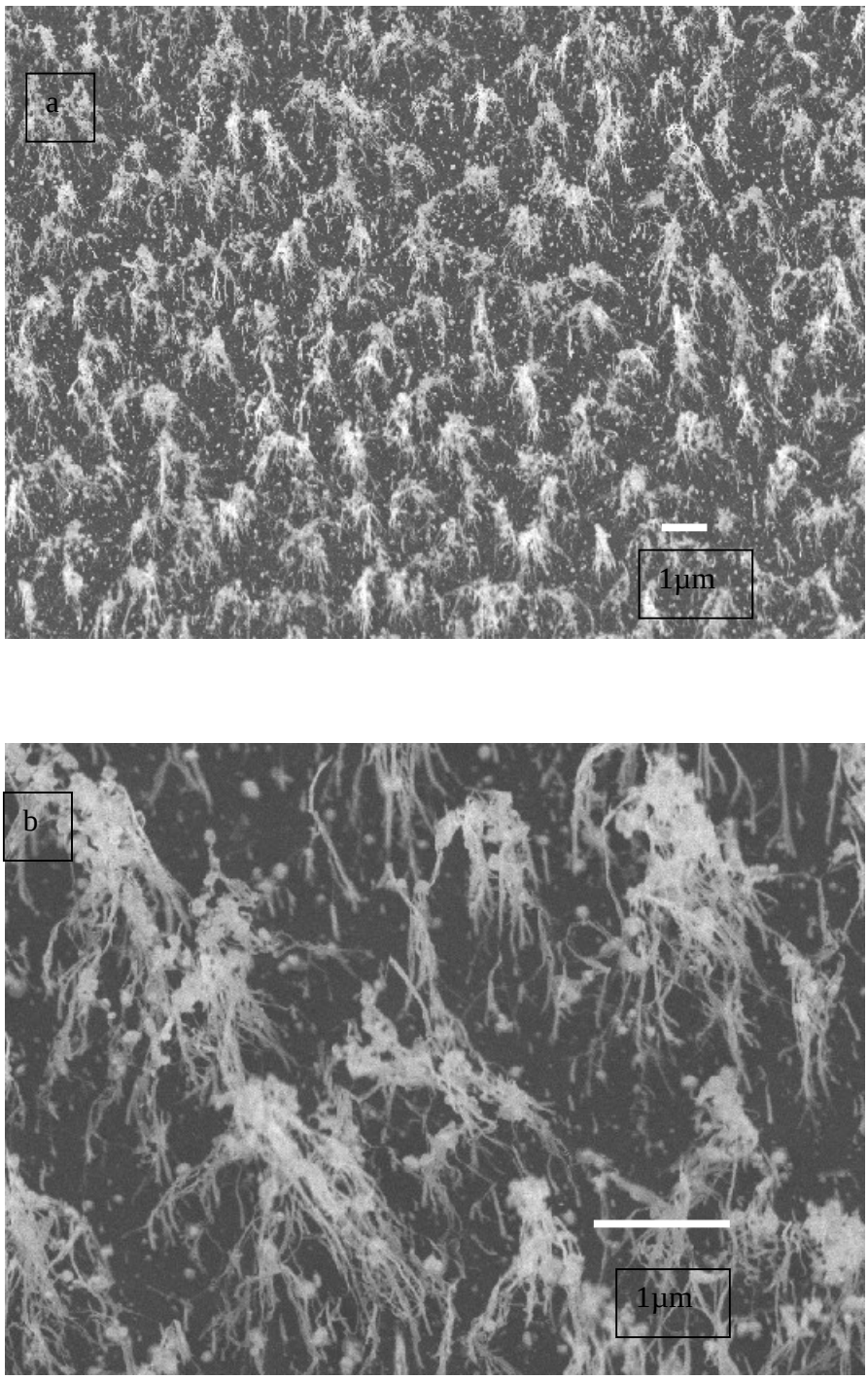

Fig. 4.4(a): SEM image of random MWNT after 10min plasma treatment with Ar (CNT-Ar10min). (b): High magnification SEM of the same sample.

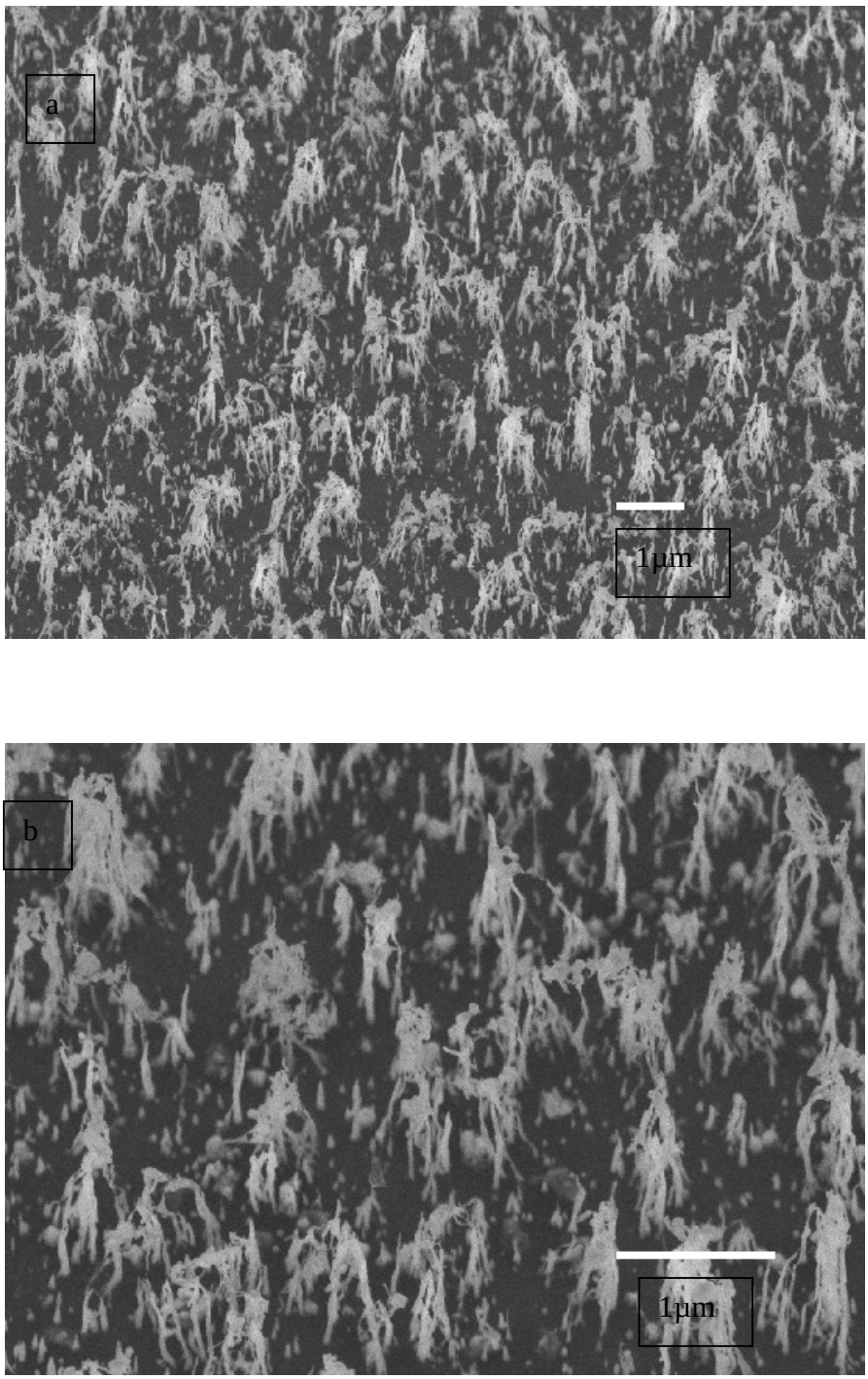

Fig. 4.5(a): SEM image of random MWNT after 20min plasma treatment with Ar (CNT-Ar20min). (b): High magnification SEM of the same sample.

From the SEM images, we can see that the plasma etching process does cause structural changes to the random MWNTs. In general, we can see that the nanotube lengths become increasingly shorter with increasing etching time. The nanotube density decreases and the random MWNTs bundle together to form arrays of vertically aligned nanotube bundles. Each bundle consists of several nanotubes that are joined at their tips. Several large particles cap the top of each bundle, which are the bright particles in the SEM images. These particles have been identified as iron catalyst particles using TEM with EDX analysis function. It also can be observed that the rate of etching is greater for Ar than N_2 as the MWNTs treated with Ar plasma has lower density and are shorter in length compared to that treated with N_2 after equivalent treatment times.

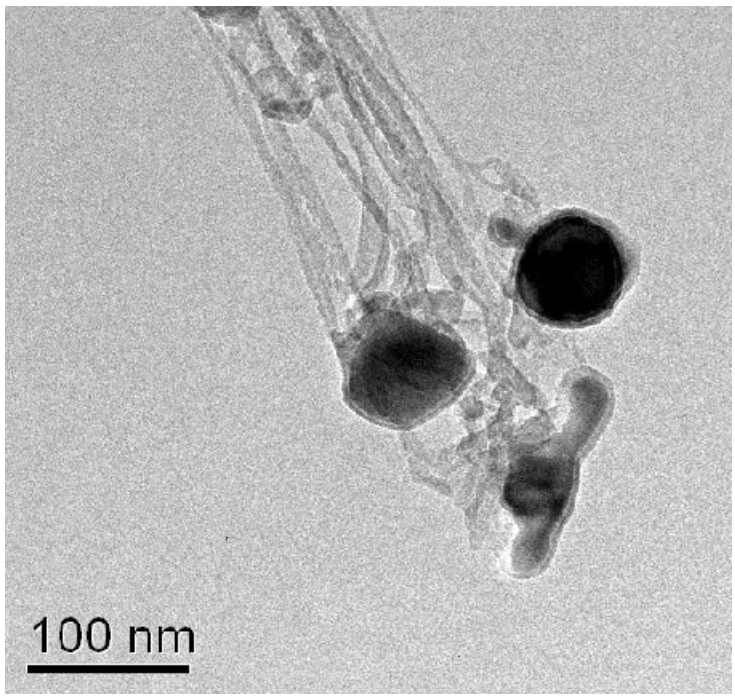

Fig. 4.6: TEM image of MWNT after 10min Ar plasma etching. The image clearly shows the bundling effect and the dark iron catalyst particles that cap the bundle.

After SEM characterization, we next placed the respective samples into the 'homemade' chamber and measured the field emission characteristics at a maximum applied voltage of 450V. Results of the measurement are shown in Fig. 4.7.

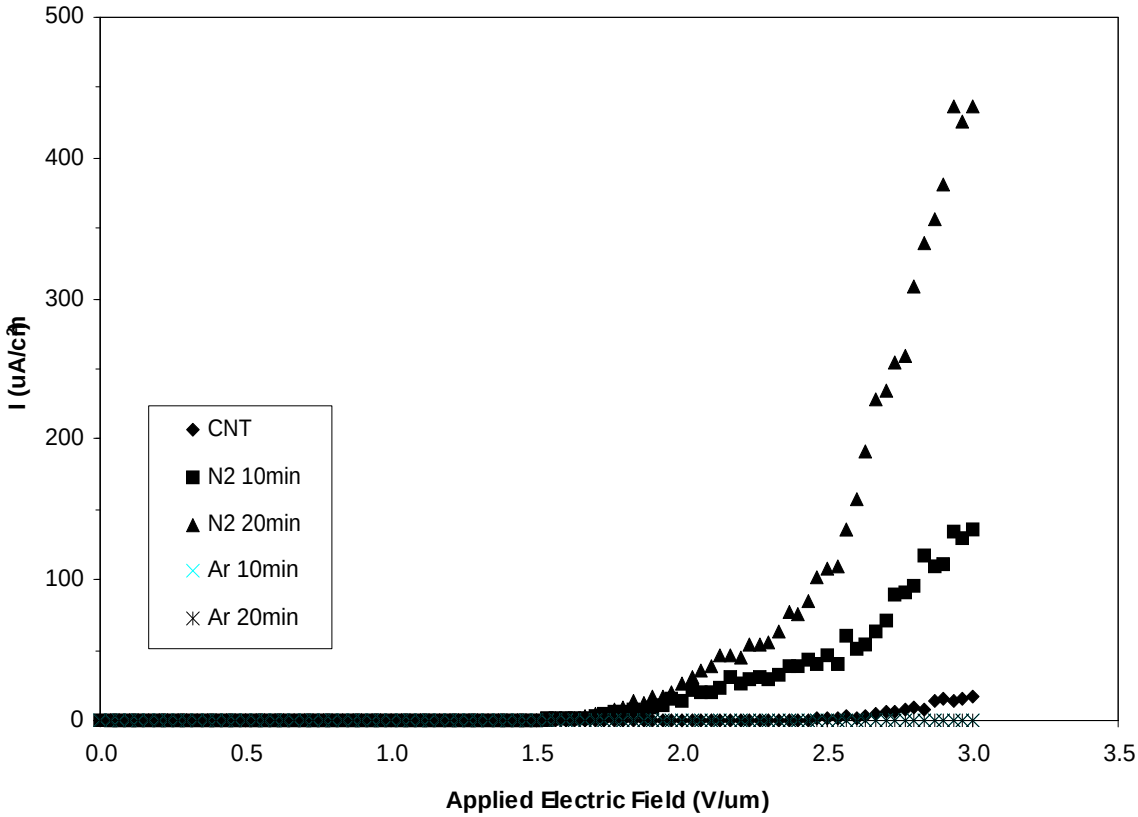

Fig. 4.7: Field emission of random MWNTs, CNT-N10min, CNT-N20min, CNT-Ar10min and CNT-Ar20min. It can be seen clearly that CNT-N20min has the best field emission properties. Inset shows the corresponding F-N plot.

From Fig. 4.7, both N_2 treated MWNTs samples show improved field emission compared to the unmodified MWNTs, with CNT-N20min showing the best characteristics. CNT-N20min displays the lowest turn-on voltage and highest emission currents at 450V applied field. On the other hand, both CNT-Ar10min and CNT-Ar20min show poorer

field emission characteristics compared to the untreated MWNTs. In fact, both Ar treated MWNTs show only negligible field emission currents at 450V. Hence, it can be seen that plasma treatment of MWNTs with N_2 and Ar does in fact modify their field emission properties significantly. We shall now attempt to investigate the physical and chemical modifications that occur as a result of the etching process in order to explain these observations.

4.3.1 N_2 Treated MWNTs

The F-N plot for the field emissions of pure MWNT, CNT-N10min and CNT-N20min are shown in Fig. 4.8.

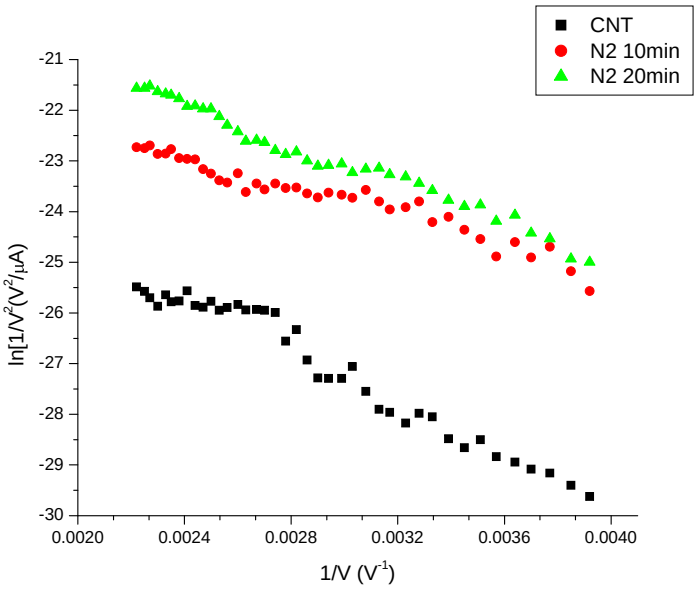

Fig. 4.8: F-N plots of field emission of MWNT, CNT-N10min and CNT-N20min.

As we can see, the F-N plot shows linear relationship, thereby providing evidence that the emission follows the F-N theory. Thermionic emission should not play a part here since we did not supply heat during our experiments. Chen *et al*. had recently

reported that thermionic emission is only significant at high temperatures of about 700K (2). Table 1 below gives a summary of the field emission characteristics of the three samples. CNT-N20min has a turn-on voltage that is almost 1V lower than MWNT while the emission current at 3V/μm is almost 30 times higher.

Sample	Turn-on Field (V/μm)	Emission at 3V/μm (μA/cm^2)
MWCNTs	2.67	16.5
CNT-N10min	1.77	140
CNT-N20min	1.73	450

Table 1.

The enhancement of field emission after N_2 treatment can be due to both physical and chemical changes that take place in the MWNTs during the etching process. As seen in the previous sections, the N_2 plasma causes the nanotube density to decrease and the nanotube length to be shortened. There have been various reports that densities and orientations of the nanotubes affect the emission (3, 4). A high-density film shows decrease in emission quality compared to one that has medium density. This is due to screening effects. When the intertube distance is sufficiently large, the field amplification factor is governed just by the dimensions of the MWNT, that is, its diameter and length. However, when the intertube distance decreases, then screening effect becomes significant.

Electrostatic calculations have shown that the field amplification factor begins to decrease once the intertube distance is twice the height of the carbon nanotubes and drops rapidly for further decreasing distances (1). However, the nanotubes cannot be too far

apart as well since number density of emitters decrease with increasing intertube distance. If there are too few emitters then the nanotube film becomes an ineffective cathode. Following the above argument, one can also enhance the field emission quality by shortening the nanotubes, as this will also decrease the screening effect. This also explains why CNT-N20min shows better emission than CNT-N10min since the density and length of CNT-N20min is both lesser than for CNT-N10min.

Further information of the structural effects can be obtained by Raman spectroscopy. Fig. 4.9 below shows the Raman spectroscopy spectrums for all five samples.

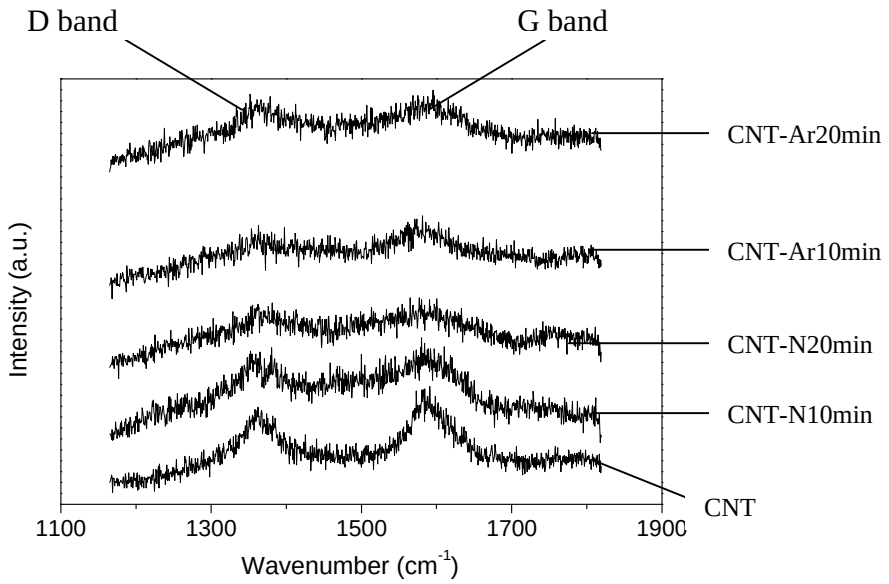

Fig. 4.9: Raman spectroscopy measurements of unmodified MWNTs, CNT-N10min, CNT-N20min, CNT-Ar10min and CNT-Ar20min. The left peak is associated with the D-band and the right peak is associated with G-band.

The G peak is reported to indicate crystalline graphite while the D band is associated with sp^3 carbon and defects in the curved graphite sheets (5). Hence, an increase in the ratio of the intensity of the D peak (I_D) to the intensity of the G peak (I_G) indicates an increase in

the density of structural defects. Table 2 lists the relative intensities of the D and G peaks of unmodified MWNT, CNT-N10min and CNT-N20min and their respective intensity ratios.

Sample	$I_{D/counts}$	$I_{G/counts}$	I_D/I_G
MWNT	139	158	0.88
CNT-N10min	190	203	0.94
CNT-N20min	235	239	0.98

Table 2 Relative intensities of the D-band and G-band from Raman Spectroscopy.

I_D/I_G is the largest for CNT-N20min as expected since the plasma treatment time is the longest, implying that it has the greatest density of structural defects of the three samples. Since each defect can serve as an emitter site, this would imply that CNT-N20min has the greatest number of emitter sites per nanotube, followed by CNT-N10min and finally by MWNT. This supports the observation that CNT-N20min has the greatest emission current density at 3V/μm.

Besides looking at the physical changes, chemical modifications of the MWNTs are also induced by the etching process, since N is reactive. Using a synchrotron radiation source (Singapore Synchrotron Light Source), we conducted photoelectron emission spectroscopy (PES) to investigate the work function F of the pure and N_2 plasma treated MWNTs together with a thin gold film that is sputter deposited on a Si(100) substrate. This is to facilitate the location of the Fermi level, which is clearly evident in a pure metal PES spectrum. Moreover, all four samples are in electrical contact with each other, hence, their Fermi levels will be aligned with one another. Fig. 4.10 shows how we

determine *W* from the PES spectrum which is required in Equation (6) for the calculation of the workfunction *F* .

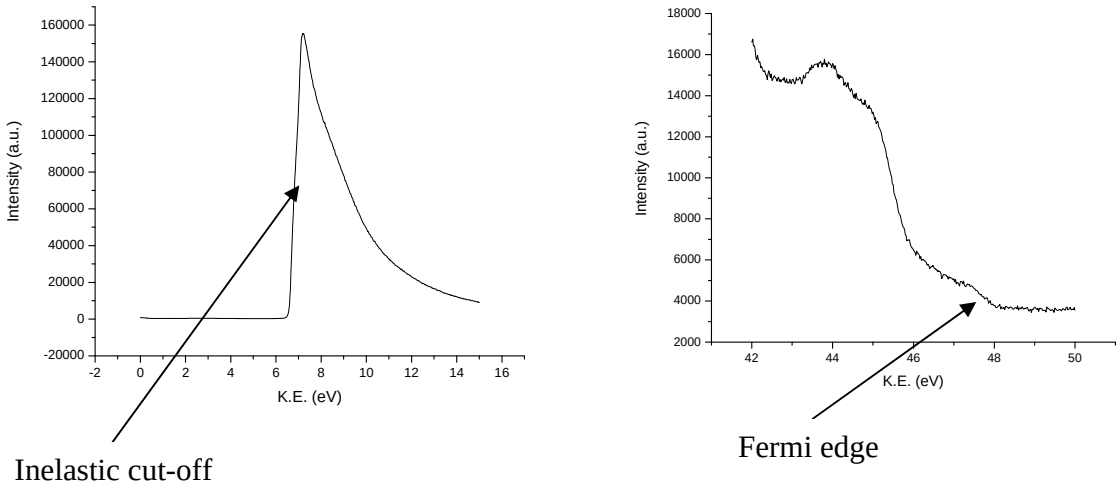

Fig. 4.10: Shows parts of a typical PES spectrum. W is given by the energy width between the Fermi edge and inelastic cut-off.

The workfunction measurement results are tabulated in Table 3.

Sample	F *(eV)*
MWCNTs	4.20± 0.02
CNT-N10min	4.14± 0.02
CNT-N20min	4.32± 0.02

Table 3.

As expected, the workfunction of CNT-N10min is lower than that of MWNT since it shows lower turn-on fields. The lowering of the workfunction is probably due to the higher degree of C sp^3 bonding present in SNT-N10min compared to MWNT, as inferred from the Raman spectroscopy results. As a result of the increase in sp^3 bonding, the

effective energy barrier of electron emission becomes closer to that of diamond, which has a negative electron affinity that allows for a low energy threshold for electrons escaping from the conduction band to the vacuum (5). This in turn results in a reduction in the turn-on field (5).

However, CNT-N20min actually has a higher than expected workfunction, which contradicts our Raman spectroscopy observations that show that CNT-N20min has a higher sp^3 bond concentration than CNT-N10min. This evidence is further confirmed by the XPS measurements of the two samples, shown in Fig 4.11. Both samples show peaks at 398.2eV, 398.6eV, 399.7eV and 400.8eV, which correspond to C-N, C=N (sp^3 bonding), C=N (sp^2 bonding) and NO. There is also a peak at 402.5eV present in both spectrums, which we suspect to be interstitial N. This peak has been observed in previous reports studying nitrogenated carbon but was not identified (6). The XPS spectrum for CNT-N20min has an additional peak that corresponds to nitrided Fe at 396.1eV.

From the XPS spectra, we can calculate the ratio of the sp^3 bonded C to the sp^2 bonded C, which is 0.76 for CNT-N10min and 1.05 for CNT-N20min. Thus, the amount of sp^3 bonding in CNT-N20min is higher than in CNT-N10min. This suggests that the workfunction for CNT-N20min should be lower than both MWNT and CNT-N10min, using the previous argument.

A reason for this discrepancy is probably because the large distances between the nanotube bundles of CNT-N20min, and PES actually measures the workfunction of the exposed Fe/Si substrate as well instead of just that of the treated nanotubes. The presence of the nitrided Fe peak in the XPS of CNT-N20min that was previously absent in the CNT-N10min spectrum also lends weight to the argument.

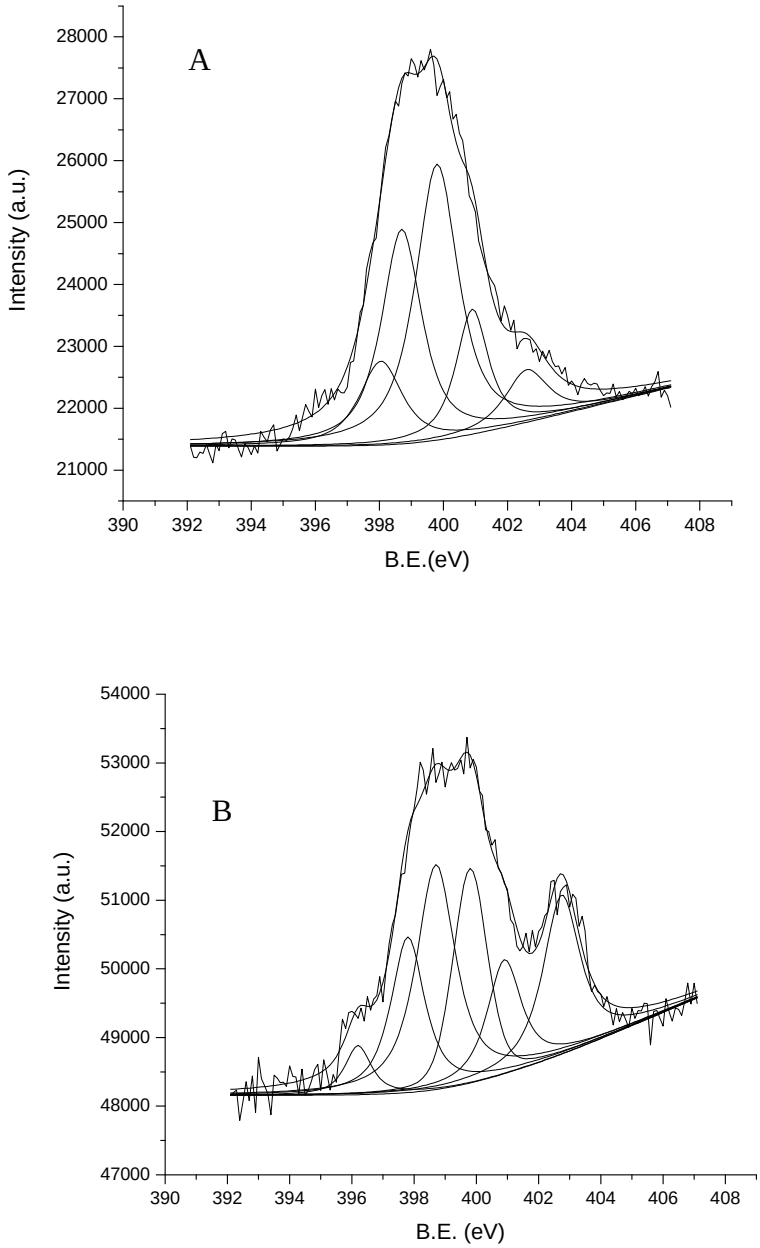

Fig. 4.11: (A) XPS spectrum of CNT-N10min. (B) XPS spectrum of CNT-N20min.

We measured the workfunction of a bare Fe/Si substrate that has been annealed to the same temperature as that during nanotube growth. The measured work function is

found to be 4.59eV. Hence, this provides a plausible explanation as to why our measured workfunction of CNT-N20min is higher than expected.

4.3.2 Ar Treated MWNTs

Ar, being inert, will only modify the MWNTs physically and not chemically. Hence, the work function of the Ar plasma etched MWNTs should be the same as that of the pre-etched MWNTs. Due to the lack of chemical effect, XPS was also not pursued. Unlike the MWNTs that were treated with N_2, CNT-Ar10min and CNT-Ar20min both showed successively worse field emission characteristics compared to unmodified MWNTs. In fact, CNT-Ar20min showed almost no field emission at 3V/μm. The Ar atom is more massive compared to the N atom, and hence, Ar will etch at a faster rate. It is possible that after 10mins of Ar etching, the Ar plasma has already caused significant structural damage to the MWNTs. There has been reports whereby excessive exposure to Ar etching results in a degradation in the field emission of the nanotubes, as the nanotubes are structurally damaged to the point where they are no longer effective cathodes (7). This is probably due to the destruction of emitter sites on the nanotubes, thereby making it difficult for field emission to take place. From Fig.4.4 and Fig.4.5, we indeed observe greater structural damage to the nanotubes than compared those treated with N_2 in Fig. 4.2 and Fig. 4.3.

4.4 Conclusion

In this project, we have successfully demonstrated that plasma etching is an effective process for enhancing the field emission characteristics of carbon nanotubes. Using N_2 plasma, we are able to observe lowering of the turn-on fields by up to 1V and

emission current density increase by almost 30 times compared to untreated MWNTs. The reasons for this have been determined to be not only because of the shortening of the nanotube length and reduction in density, but also due to the lowering of the workfunction of the treated MWNTs through the formation of sp^3 bondings in the structure of the nanotube. The same success is not observed when using Ar as the etching agent under the same conditions. This is due to the much higher rate of etching of Ar compared to N_2, which resulted in the nanotubes being excessively damaged to the state where they are no longer effective field emitters.

This work has great impact in the development of effective field emission cathodes. By using a simple plasma treatment, we have further enhanced the field emission characteristics of a material with already very good field emission properties. Much work still has to be done so as to determine the optimum conditions for the etching process so as to achieve the best enhancements, since prolonged treatment can lead to adverse damage to the cathode. With continual efforts, cheap field emission displays with low operating voltages will soon be a reality.

Chapter 4

References:

1) Bonard, J-M., *et al.*, *Solid State Electronics*, **45,** 893 (2001).

2) Chen, J., *et al*. *Appl. Phys. Lett.*, **83**, 746 (2003)

3) de Pablo, P. J., *et al.*, *Appl. Phys. Lett.*, **75**, 3941 (1999).

4) Ebbsen, T. W., *Nature*, **367**, 519 (1994).

5) Yu, K., *et al.*, *Chem. Phys. Lett.*, **373**, 109 (2003).

6) Laskarakis, A., *et al. Diamond and Related Mat.*, **10** 1179 (2001).

7) Kyung, S. A., *et al.*, *Carbon*, **41**, 2481 (2003).

Chapter 5: Conclusion

The discovery of carbon nanotubes is indeed a phenomenal one. With its myriad of fantastic properties, the potential of carbon nanotubes is really quite limitless. However, it is still quite a long way till carbon nanotubes can effectively realise its potential and be readily used in actual applications and devices.

In the first part of this thesis, we have demonstrated a method to enhance the optical liming prowess of MWNTs by coating the nanotubes with a thin layer of noble metal nanoparticles. This is certainly an exciting discovery, as pure MWNTs are already known to shown excellent optical limiting characteristics. And now we are actually able to further enhance this characteristic, this new composite material really has great prospects in optical applications, such as sensor protectors and optical switches. There is still much work to be done in this area however. First of all, the coating technique of the nanoparticles onto the nanotubes needs to be optimised. In this project, our coated nanoparticles had a very large size distribution. If a more uniform size distribution can be achieved then perhaps the optical limiting enhancement will be stronger than observed. Secondly, the ultrasonic process for removing the coated nanotubes from the Fe/Si substrate is destructive to the coating; hence it would be better if there is an alternative method. Lastly, there are still many other optically active materials that can be coated onto the MWNTs. It is worth trying these materials as well to see if better enhancements can be achieved.

The second part of the project showed that plasma etching of MWNTs can significantly enhance their field emission characteristics. We used N_2 plasma to modify the MWNTs physically and structurally, thereby reducing the turn-on field and also the

current emission density. This is important for the progress of MWNTs as cathodes in field emission displays. Although we tried to achieve the same effects with Ar etching, we got negative results due to the high etching rates of Ar, which led to the destruction of the emitter sites on the nanotubes that caused poorer field emission techniques. Future work that can be done includes optimising the etching process as well as searching for alternative etching agents.

Acknowledgements

Firstly, I would like to thank sincerely A/Prof Andrew Wee of the Physics Department of National University of Singapore who has been my supervisor since my first UROPS project till my Master's thesis. I am really grateful for his faith in me, in letting me have full control over the direction of my thesis, while constantly making sure that I was doing fine. Despite being extremely busy with his commitments, he always found time to help me patiently. And it was only his kind understanding that allowed me to do my Master's course in one year instead of the usual two.

Secondly I would like to thank A/Prof Ji Wei for his advices on the optical limiting aspect of my projects and for his valuable inputs and suggestions. I would also like to thank Asst/Prof Sow Chorng Haur for all the great chats we had about project ideas and directions. I also thank him for letting me use his lab facilities, especially the field emission system. Dr Gao Xingyu has been very helpful in my experiments at the Singapore Synchrotron Light Source.

Thirdly, I would like to thank Chin Kok Chong for working with me during the project and also a constant companion and a good friend. I could always count on him for helps and advice. I would like to thank Chen Weizhe for helping me with my optical limiting measurements and all the related experiments. I would also like to thank Mr Zhu Yanwu for all his help in my field emission experiments and also being such a great classmate. Getting to know both Yanwu and Weizhe has certainly been one of the highlights this year.

To all those who have made my Master's year such an enjoyable experience, especially Ghee Lee and Cheong, thank you for making the lab such entertaining places.

Also, many thanks to my good friends Say Tiong, Jihan, and Yuling for their encouragement and support.

Finally I would like to thank my girlfriend Liwei for being so supportive and encouraging during this trying period. She gave me my strength to go on. Last but not least, I thank my parents for the patience with me and my constant mood swings. Without them, I would not be here today; I would never have had the strength to go this far…